

# EMPDF: Inferring the Milky Way mass with data-driven distribution function in phase space

Zhaozhou Li,<sup>1,2,3</sup>★† Jiaxin Han,<sup>1,3,4</sup> Wenting Wang,<sup>1,3,4</sup> Yong-Zhong Qian,<sup>5</sup> Qingyang Li,<sup>1,3,4</sup>  
Yipeng Jing,<sup>1,3,4,6</sup> Ting S. Li<sup>7</sup>

<sup>1</sup> Department of Astronomy, Shanghai Jiao Tong University, Shanghai 200240, China

<sup>2</sup> Centre for Astrophysics and Planetary Science, Racah Institute of Physics, The Hebrew University, Jerusalem, 91904, Israel

<sup>3</sup> Shanghai Key Laboratory for Particle Physics and Cosmology, Shanghai 200240, China

<sup>4</sup> Key Laboratory for Particle Astrophysics and Cosmology (MOE), Shanghai 200240, China

<sup>5</sup> School of Physics and Astronomy, University of Minnesota, Minneapolis, MN 55455, USA

<sup>6</sup> Tsung-Dao Lee Institute, Shanghai Jiao Tong University, Shanghai, 200240, People's Republic of China

<sup>7</sup> Department of Astronomy and Astrophysics, University of Toronto, 50 St. George Street, Toronto ON, M5S 3H4, Canada

## ABSTRACT

We introduce the EMPDF (Empirical Distribution Function), a novel dynamical modeling method that infers the gravitational potential from kinematic tracers with optimal statistical efficiency under the minimal assumption of steady state. EMPDF determines the best-fit potential by maximizing the similarity between instantaneous kinematics and the time-averaged phase-space distribution function (DF), which is empirically constructed from observation upon the theoretical foundation of oPDF (Han et al. 2016). This approach eliminates the need for presumed functional forms of DFs or orbit libraries required by conventional DF- or orbit-based methods. EMPDF stands out for its flexibility, efficiency, and capability in handling observational effects, making it preferable to the popular Jeans equation or other minimal assumption methods, especially for the Milky Way (MW) outer halo where tracers often have limited sample size and poor data quality. We apply EMPDF to infer the MW mass profile using *Gaia* DR3 data of satellite galaxies and globular clusters, obtaining consistent measurements with the constraints from simulation-informed DF fitting (Li et al. 2020). While the simulation-informed DF offers superior precision owing to the additional information extracted from simulations, EMPDF is independent of such supplementary knowledge and applicable to general tracer populations. We provide tabulated measurements of the mass profile from EMPDF, along with updated measurements from simulation-informed DF.

**Key words:** Galaxy: halo – Galaxy: structure – Galaxy: kinematics and dynamics – galaxies: dwarf – dark matter

## 1 INTRODUCTION

Gravity is the predominant force in shaping cosmic structures. A fundamental task in galactic dynamics is dynamical modeling, determining the underlying mass distribution (equivalently gravitational potential  $\Phi$ ) from the kinematics of a set of tracers assumed to be in equilibrium. The mass distribution is typically characterized by some parameters to be estimated. The *Gaia* mission (2016) has recently made it possible to acquire nearly complete 6D kinematic data (positions  $\mathbf{r}$  and velocities  $\mathbf{v}$ ) for tracer populations of the Milky Way (MW). This significant advancement not only enables more accurate measurements of the MW's mass distribution (see Wang et al. 2020 for a comprehensive review), but also necessitates developing new methodologies to fully exploit the data.

The 6D phase-space distribution function (DF) provides a complete description of steady-state systems (Binney & Tremaine 2008, BT08 hereafter). Ideally, if we have a model for the expected DF of tracers in arbitrary potential,  $f(\mathbf{r}, \mathbf{v} | \Phi)$ , the best-fit potential can be

derived with optimal statistical efficiency. Most dynamical modeling methods rely on DFs in some form, although some methods use only part of the information contained in the full DF. For example, the *Jeans equation* uses moments of the DF (tracer density and velocity dispersion profiles), thereby losing information from higher-order moments (see Łokas & Mamon 2003; Evslin & Del Popolo 2017; Read et al. 2021). This limitation also applies to mass estimators based on the Jeans equation (aka. virial estimators, e.g., Bahcall & Tremaine 1981; Walker et al. 2009; Wolf et al. 2010; Watkins et al. 2010). Similarly, the *escape velocity* method only considers a small fraction of stars in the tail of the velocity distribution (Caldwell & Ostriker 1981; Leonard & Tremaine 1990). Therefore, using the full DF is expected to provide tighter constraints. Moreover, observational errors and incompleteness can be naturally incorporated into DF models via forward modeling, which is nontrivial for many other methods.

Yet finding the appropriate DF model for a given tracer population is a challenging task. Various approaches exist to construct DF models analytically, including the Eddington (1916) inversion of density profiles with assumed velocity anisotropy (e.g., Osipkov

★ zhaozhou.li@mail.huji.ac.il; lizz.astro@gmail.com

† Marie Skłodowska-Curie Fellow

1979; Merritt 1985; Cuddeford 1991; Gerhard 1991; Wojtak et al. 2008) and analytical functions of orbital integrals (e.g., energy and angular momentum: Michie & Bodenheimer 1963; Kent & Gunn 1982; Evans et al. 1997; Gieles & Zocchi 2015; actions: Binney & McMillan 2011; Ting et al. 2013; Binney 2014; Posti et al. 2015; Trick et al. 2016; Vasiliev 2019; Binney & Vasiliev 2023). Several DF models have been employed to infer the MW mass (e.g., Wilkinson & Evans 1999; Eadie et al. 2018; Deason et al. 2021; Wang et al. 2022a; Slizewski et al. 2022; Shen et al. 2022). A major concern of such presumed analytical DFs is that they may not accurately represent specific tracer populations, potentially leading to substantially biased results (Wang et al. 2015a; Han et al. 2016b).

A more realistic approach uses template DFs derived from numerical simulations. Li et al. (2017) developed a method to rescale the orbital distribution of satellite galaxies in simulations to different halo masses, which was applied to estimate the MW halo mass by Callingham et al. (2019). However, this method is biased and requires additional calibration because it uses the likelihood of orbits instead of direct observables ( $\mathbf{r}, \mathbf{v}$ ). Li et al. (2019) resolved this issue by further deriving the full phase-space DF arising from the satellite orbits under the steady-state assumption (Han et al. 2016a), with which Li et al. (2020a) obtained one of the most reliable mass constraints on the MW outer halo. The MW virial mass is inferred with a statistical uncertainty of 20% and systematics  $\leq 10\%$ . While this technique offers optimal statistical efficiency (see §3.3), it is limited to tracers that are well-understood in simulations, such as satellites.

Concerns about model dependence in the above methods have prompted the development of more flexible DF models with large degrees of freedom to adequately describe realistic tracers. The *orbit superposition* method describes the DF using a library of discrete orbits (Schwarzschild 1979; van den Bosch et al. 2008; McMillan & Binney 2012; Zhu et al. 2018; Vasiliev & Valluri 2020) or a series of basis functions (e.g., BT08, eq. 4.116, Bovy et al. 2010; Magorrian 2014, 2019) with adjustable weights. Recently, machine learning techniques such as normalizing flows have been introduced to construct highly flexible models (Green & Ting 2020; Green et al. 2023; An et al. 2021; Naik et al. 2022; Buckley et al. 2023; Lim et al. 2023). In general, such flexible models with numerous free parameters are computationally demanding and often rely on ad-hoc regularization to mitigate parameter degeneracy.

Another appealing approach is to use the observed tracers themselves as the orbit library, thus eliminating the need for assumptions on the functional form of the DF and avoiding ad-hoc construction and regularization of orbit libraries. The main idea is that a steady-state system does not evolve over time when moving the tracers along their orbits under the correct potential. Therefore, the similarity between the instantaneous observation and time-averaged statistics in a trial potential represents its goodness of fit. As steady-state is the only essential assumption here, such methods can be dubbed as *minimal assumption* methods. An example is the orbital roulette method (Beloborodov & Levin 2004, also cf. Price-Whelan et al. 2021), which compares the phase angle distribution of tracers with a uniform distribution (as expected for time average). A natural step forward is to compare the full 6D DF with the maximal available information.

Taking the time average is equivalent to dispersing each particle according to the travel time distribution along its orbit, aka. the orbital Probability Density Function (oPDF, Han et al. 2016a),  $dP(\lambda|\text{orbit}) \propto dt$ , where  $\lambda$  denotes position in orbit. Han et al. (2016a) showed that the oPDF principle is the microscopic equivalence to the macroscopic condition of steady-state, the Jeans theorem, or the so-called “random phase principle” (Beloborodov & Levin

2004, where the phase angle is a proxy for the travel time). Summing up the oPDFs sampled along each tracer’s orbit then provides an empirical realization of the time-averaged 6D DF (see also §2.1). However, the discreteness in the distribution of tracer orbits prevents direct comparison between this DF and observation. To circumvent this difficulty, the oPDF method<sup>1</sup> by Han et al. (2016a) marginalizes orbital distribution and considers the likelihood between the observed radial distribution of tracers and its time average.

In this work, we develop a new method, eMPDF (empirical DF). It is a natural extension of the oPDF method, but constructs a continuous empirical time-averaged DF nonparametrically from discrete tracers under the trial potential, allowing direct comparison with observations. The key difference from oPDF is that it replaces the discrete orbit distribution in oPDF with a smooth distribution using kernel density estimation (KDE). The likelihood between the empirical DF and the observation sample then enables Bayesian inference for the true potential well. As shown in this paper, the new eMPDF method is intuitive, efficient, flexible, and simple to implement.

eMPDF shares some spirits with the orbit superposition methods (cf. Han et al. 2016a §6.3), especially Magorrian 2014 (see comments in Appendix A2), but is much easier to implement and compute. Unlike the orbit superposition methods, eMPDF does not involve free parameters such as adjustable weights for the orbital library or any ad-hoc regulating procedures. Beraldo e Silva et al. (2024) recently proposed a method based on minimum entropy in action space, bearing a similar mathematical expression to the likelihood used in eMPDF, despite the distinct physical motivations. We argue that eMPDF represents a more fundamental framework where the minimum entropy principle can be derived as a phenomenological result (§5.1).

The high efficiency of eMPDF enables its application to very small tracer samples with reasonable precision. As a DF method, it also facilitates the handling of the observational selection function. For the first demonstration, we apply this method to infer the MW mass using globular clusters and satellite galaxies as tracers (§4).

The layout of this paper is as follows. We present the eMPDF method in §2. Its validity and performance are evaluated using mock samples and compared to other methods in §3. We apply eMPDF to estimate the MW mass profile in §4. Possible future extensions are discussed in §5, followed by conclusions in §6.

Throughout this paper, the abbreviation “DF” exclusively represents the 6D phase-space *distribution function*,  $f(\mathbf{r}, \mathbf{v})$ . For the probability distribution of other quantities ( $X$ ), we simply use “distribution”, denoted as  $p(X) \equiv dP/dX$ . Specifically, the *orbital distribution* refers to the distribution of orbits in terms of orbital integrals, e.g.,  $p(E, L) \equiv d^2P/dEdL$  and should not be confused with oPDF. We denote  $\mathbf{w} \equiv (\mathbf{r}, \mathbf{v})$  for the 6D phase space coordinates. The halo mass  $M_h$  refers to the *total* mass (including baryons) enclosed by the radius  $R_h$ , within which the average density is 200 times the critical density of the present universe,  $\rho_{\text{crit}} = 3H_0^2/(8\pi G)$ , with  $H_0 = 70 \text{ km s}^{-1} \text{ Mpc}^{-1}$  and  $G$  the gravitational constant. We use  $M_{200c}$  instead of  $M_h$  for clarity when referring to the MW mass.

<sup>1</sup> We use oPDF to refer to the conditional distribution,  $dP(\lambda|\text{orbit}) \propto dt$ , while oPDF refers to the radial likelihood method based on the oPDF principle in Han et al. (2016a).

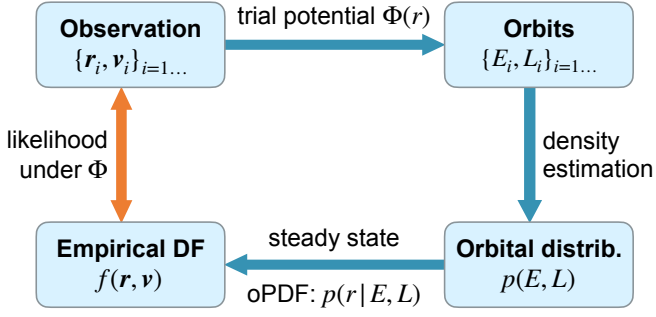


**Figure 1.** Flowchart of the EMPDF method. The best-fit parameters of the potential can be inferred by maximizing the likelihood (minimizing KL divergence) between the observed instantaneous kinematics,  $\{r_i, v_i\}$ , and the time-averaged DF,  $f(r, v)$ , constructed empirically from observation under the trial potential. Other orbital integrals such as actions can be used instead of  $(E, L)$  to extend this method for non-spherical systems.

## 2 DYNAMICAL MODELING WITH EMPIRICAL DF

We aim to infer the potential  $\Phi(r)$ , which is specified by a set of free parameters  $\Theta_\Phi$ , from the 6D kinematics  $\{r_i, v_i\}_{i=1}^N$  of a tracer sample observed within a radial range  $r_{\min} < r < r_{\max}$ .

Same as oPDF, the EMPDF method is based on the minimal common assumptions that the tracers are in *steady state* and the potential is *static*. While the general idea of EMPDF can be applied to less symmetrical potentials (see §5), this paper focuses on *spherical potentials*, where the tracers therein can nevertheless follow arbitrary symmetry or velocity anisotropy.

The main idea of EMPDF is that the underlying DF of tracers does not change over time under the steady-state assumption. If we evolve the tracers along their orbits in the *correct* potential, the kinematics at an arbitrary epoch or the time-averaged distribution is expected to be statistically the same as the observed instantaneous kinematics. Therefore, we can infer the potential through the following procedures (see flowchart in Fig. 1):

- Construct the time-averaged DF of the tracers empirically in given trial potential (§2.1);
- Find (the parameters of) the best-fit potential that maximizes the similarity between this empirical DF and the observation (§2.2).

Taking advantage of the complete DF, observational selection (i.e., incompleteness, §2.3) and measurement errors (§2.4) can be incorporated when necessary.

To illustrate this idea, we generate 1000 mock tracers in equilibrium for an NFW halo (Navarro et al. 1996) of  $M_h = 10^{12} M_\odot$  with a fixed concentration  $c = 10$  (see §3.1). We then evolve these tracers in different trial potentials and compute their time-averaged statistics. As expected, the time-averaged distribution in the correct potential matches best with the instantaneous observation across all dimensions shown in Fig. 2. In contrast, when placed in a potential shallower (deeper) than the true one, the tracers appear to crowd around their pericenter (apocenter) with a non-uniform phase angle distribution and tend to expand (contract) in space over time.

The time-averaged DF can be compared to observations in different dimensions, such as the mean phase angle,  $\langle \theta \rangle$ , the phase angle distribution (Beloborodov & Levin 2004, orbital roulette),  $p(\theta)$ , the spatial distribution (Han et al. 2016a, oPDF),  $p(r)$ , and the 6D DF (EMPDF),  $f(r, v)$ . We refer the readers to Han et al. (2016a) for a summary and public implementation<sup>2</sup> of these minimal assumption

<sup>2</sup> <https://github.com/Kambrian/oPDF>

methods except for EMPDF. The proposed EMPDF is expected to have optimal efficiency of its kind by fully exploiting the complete 6D DF.

### 2.1 Constructing the empirical DF

In a spherical potential  $\Phi(r)$ , an orbit is characterized by specific energy,  $E = \Phi(r) + \frac{1}{2}(v_r^2 + v_t^2)$ , and angular momentum,  $L = r \times v$ , where  $v_r$  and  $v_t$  are the radial and tangential velocities respectively. When the tracer distribution is also spherically symmetric, only  $L = |L|$  matters, and the phase space coordinate of a particle can be fully specified by  $(r, E, L)$ . One can also use other orbital integrals instead, such as actions (§5.1). The resultant DF  $f(r, v)$  does not depend on the particular choice. Here we adopt  $(E, L)$  for the ease of computing.

The normalized phase-space DF,  $f(r, v) \equiv d^6P/d^3r d^3v$ , can be decomposed into two parts, the *orbital distribution*,  $p(E, L) \equiv d^2P/dEdL$ , and the *conditional radial distribution* along each orbit,  $p(r | E, L)$ , as

$$f(r, v) = \frac{|v_r|}{8\pi^2 L} p(r | E, L) p(E, L), \quad (1)$$

where the first term on the right-hand side is the Jacobian due to change of variables (see Appendix A of Li et al. 2019).

Han et al. (2016a) proposed to model the orbital distribution empirically as  $p(E, L) = \frac{1}{N} \sum_{i=1}^N \delta(E - E_i, L - L_i)$ , where  $(E_i, L_i)$  represent the  $i$ -th tracer under the trial potential, and  $\delta$  is the Dirac delta function. However, this distribution cannot be directly applied in the likelihood due to its discreteness (see Han et al. 2016a, Fig. 2). In EMPDF, we propose to estimate the underlying smooth distribution using *kernel density estimation* (KDE, Silverman 1986),

$$p(E, L) = \frac{\sum_{i=1}^N \omega_i \mathcal{K}(E - E_i, L - L_i)}{\sum_{i=1}^N \omega_i}, \quad (2)$$

where  $\omega_i$  is the weight of each tracer, which is 1 by default (but see §2.3 when involving selection function), and  $\mathcal{K}$  is the smoothing kernel with kernel size automatically determined by Scott (1979)'s rule (see technical details in Appendix A).<sup>3</sup> The orbital distribution of  $(E, L)$  is assumed to be moderately smooth yet may contain clumpy substructures, which will be resolved naturally with sufficient samples.

Under the steady-state assumption, the probability of a particle appearing at a position  $r$  along a given orbit is proportional to the time spent around (oPDF, Han et al. 2016a),  $p(r | E, L) dr \propto dt = dr/|v_r|$ . Normalizing over a radial orbital period yields

$$p(r | E, L) = \frac{1}{|v_r| T_r}, \quad (3)$$

where  $T_r(E, L) = 2 \int_{r_{\text{per}}}^{r_{\text{apo}}} dr/|v_r|$  is the radial period of an orbit moving between pericenter and apocenter  $[r_{\text{per}}, r_{\text{apo}}]$ . Starting from oPDF, another useful quantity is the radial phase angle defined through  $d\theta \propto dt/T_r$ , with  $\theta$  following a uniform distribution. As we limit the tracers to  $r \in [r_{\min}, r_{\max}]$ , one should interpret  $r_{\text{per}}$  as  $\max\{r_{\text{per}}, r_{\min}\}$  and  $r_{\text{apo}}$  as  $\min\{r_{\text{apo}}, r_{\max}\}$  throughout this paper (see Han et al. 2016a; Li et al. 2019).<sup>4</sup>

<sup>3</sup> Eq. (2) is intended for conceptual understanding and slightly different from our actual implementation, where we instead perform KDE smoothing for  $p(E, \varepsilon^2)$  and then convert it to  $p(E, L)$ . Here  $\varepsilon \in [0, 1]$  denotes the orbital circularity (see Appendix A for rationale).

<sup>4</sup> Though not obvious, this treatment is statistically equivalent to the incompleteness correction in Equations (9–11) in §2.3, as if truncating the parent sample of  $r \in [0, \infty]$  to the range  $[r_{\min}, r_{\max}]$ .

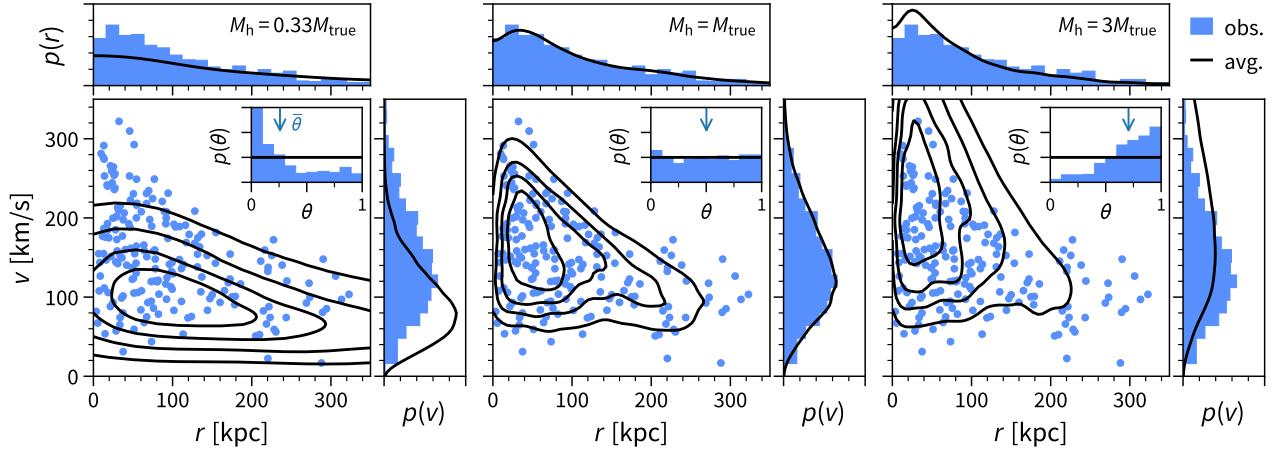


**Figure 2.** Conceptual illustration of the empirical time-averaged distribution. The instantaneous kinematics of mock tracers (blue, same in three panels) are compared to their expected time-averaged distribution (black curves) in different trial potentials (panels). The true potential is adopted in the middle panel, and a smaller (larger) trial halo mass in the left (right) panel. The projected kinematics,  $p(r, v)$ ,  $p(r)$ ,  $p(v)$ , and  $p(\theta)$ , are displayed in the main, upper, right, and inset subpanels, respectively. Here,  $r$  and  $v$  are the Galactocentric distance and velocity, and  $\theta \in [0, 1]$  is the normalized radial phase angle ( $\theta = 0$  and  $1$  for peri- and apocenter). In the main subpanels ( $v$  vs  $r$ ), the blue dots represent tracers (only 200 of 1000 are shown for clarity), while the black contours show the 20, 40, 60, 80th percentiles of the smoothed time-averaged distribution. In each inset subpanel, the arrow indicates the mean  $\theta$ . As expected, the time-averaged distribution matches best with the instantaneous observation across all dimensions under the correct potential. The proposed EMPDF method uses the likelihood of the complete 6D DF,  $f(\mathbf{r}, \mathbf{v})$ , to infer the best-fit parameters of the potential.

Combining Equations (1–3), the empirical DF of the tracer sample in a trial potential  $\Phi$  writes

$$f_{\Phi}(\mathbf{r}, \mathbf{v}) = \frac{p(E, L)}{8\pi^2 L T_r(E, L)}, \quad (4)$$

which represents the expected time-averaged distribution of the tracers. Intuitively, Eq. (4) redistributes each tracer along its orbit according to the steady-state configuration (oPDF), effectively averaging the tracer distribution over time. The DF is denoted as  $f_{\Phi}$  with a subscript  $\Phi$ , indicating its dependence on the potential (via  $E$  and  $T_r$ ). By construction, we have  $\int_{r \in [r_{\min}, r_{\max}]} f_{\Phi}(\mathbf{r}, \mathbf{v}) d^3 r d^3 v = 1$ . This DF is fully specified by  $(E, L)$  without additional dependence on  $\mathbf{r}$  or  $\mathbf{v}$ , as per the Jeans theorem (BT08, sec. 4.2).

We emphasize that the empirical DF is completely *data-driven*. There are no free parameters and no assumptions about the specific form of the DF, density profile, velocity anisotropy, or separability of DF. As Han et al. (2016a) commented, any dynamical modeling of steady-state tracers must utilize the  $p(r | E, L)$  information in some manner, though the way to handle  $p(E, L)$  can vary. There exists a continuous spectrum from fixed forms (analytical, simulation-informed) with strong prior information at risk of bias to more flexible models (Schwarzschild, Magorrian) that typically have more free parameters and ad-hoc regulation. A particularity of our EMPDF is its position at the most flexible end allowing arbitrary DFs but without free parameters, aligning with the original oPDF method. Moreover, it allows unbound orbits as long as tracers in such orbits satisfy the steady-state assumption according to Eq. (3) (e.g., in an open system with constant inflows and outflows; Han et al. 2016a).

## 2.2 Inferring the potential

Once the expected time-averaged DF is obtained empirically, we can compute the likelihood between the DF and the observed instantaneous kinematics, as the goodness of the trial potential. Maximizing the likelihood is equivalent to minimizing the statistical distance, Kullback-Leibler divergence (aka. relative entropy, see Appendix B),

between the sample and the DF. As shown in §5.1, this maximum likelihood also corresponds to the minimum entropy and maximum clustering of the *actions* of the sample.

Under a trial potential specified by parameters  $\Theta_{\Phi}$ , the probability of observing a tracer with  $\mathbf{w}_i \equiv (r_i, v_i)$  at an arbitrary epoch is

$$p(\mathbf{w}_i | \Theta_{\Phi}) = f_{\Phi}(\mathbf{w}_i), \quad (5)$$

The posterior probability of parameters for a tracer sample is then

$$p(\Theta_{\Phi} | \{\mathbf{w}_i\}) \propto p(\Theta_{\Phi}) \prod_{i=1}^N p(\mathbf{w}_i | \Phi), \quad (6)$$

where  $p(\Theta_{\Phi})$  on the right-hand side represents the prior knowledge about the parameters (constant for flat priors). One can further obtain the Bayesian evidence by integrating the right hand side over the parameter space, which is useful for model comparison (e.g., between the standard NFW potential and its contracted/cored alternatives).

The best-fit potential is then given by maximizing the posterior. We use the Bayesian optimization method (scikit-optimize, Head et al. 2021)<sup>5</sup> to search the best-fit parameters. To obtain the uncertainty and joint distribution of parameters, the common practice is to use grid scanning (efficient for one or two free parameters) or Monte Carlo sampling (e.g., Foreman-Mackey et al. 2013; Speagle 2020), which are however computationally expensive (recall that computing  $T_r$  and selection function in EMPDF involve integrations). More efficient modern techniques include the Bayesian active learning (e.g., Kandasamy et al. 2015; Acerbi 2018; El Gammal et al. 2023), which can reduce the computational cost by two orders of magnitude or more.

Tests with mock samples show that the formal error of parameters reported by our implementation slightly underestimates the actual uncertainty. This may be caused by systematics in the KDE technique. The plain KDE with a constant kernel always tends to overestimate the density around low-density points, and more so for smaller kernel sizes (e.g., when around the best fit). A more rigorous formalism should include such uncertainty of KDE. We leave

<sup>5</sup> <https://github.com/scikit-optimize/scikit-optimize>

possible technical refinements to future work but adopt an empirical correction with plain KDE in this paper. Practically, we find that using  $0.6 \ln p(\Theta_{\Phi} | \{w_i\})$  instead of the original  $\ln p(\Theta_{\Phi} | \{w_i\})$  during parameter inference provides more accurate estimate of the confidence region.

### 2.3 Incorporating selection function

Real data are often incomplete due to observational limitations, such as insufficient survey depth and sky coverage. The selection function,  $S(\mathbf{w}) \in [0, 1]$ , describes the completeness among all tracers at given phase-space locations. For example,  $S(r) = 0.5$  indicates that a tracer can only be observed/selected with half probability at  $r$ . The selection function often depends on luminosity and possibly other intrinsic properties such as color. It thus can vary for individual tracers,  $S(\mathbf{w} | \alpha_i)$ , where  $\alpha_i$  denotes the property vector of the  $i$ -th tracer that affects the selection function.

While an ensemble angular selection does not affect dynamical modeling in spherical potentials, the radial incompleteness breaks the steady state and potentially introduces severe bias. Fortunately, it is straightforward to correct the selection function in DF methods (e.g. Han et al. 2016a; Li et al. 2019; Vasiliev 2019).

The selection function affects our method in two aspects.

1. Each tracer is a biased representative of its orbit  $(E_i, L_i)$ . To account for the undetected tracers and construct the underlying orbital distribution of the complete sample, in Eq. (2) we reweigh each observed tracer with

$$\omega_i = \frac{1}{\int p(\mathbf{w}' | E_i, L_i) S(\mathbf{w}' | \alpha_i) d^6 \mathbf{w}'} \geq 1. \quad (7)$$

If not specified otherwise, the integration over the phase space is performed for the radial range  $[r_{\min}, r_{\max}]$  and arbitrary velocities.<sup>6</sup>

2. A tracer observed through its selection function follows a distribution different from the underlying DF. The likelihood then should be computed using

$$p(\mathbf{w}_i | \Theta_{\Phi}, \alpha_i) = \frac{f_{\Phi}(\mathbf{w}_i) S(\mathbf{w}_i | \alpha_i)}{\int f_{\Phi}(\mathbf{w}') S(\mathbf{w}' | \alpha_i) d^6 \mathbf{w}'} \quad (8)$$

instead of Eq. (5).<sup>7</sup>

In many cases, the selection function undergoes a sharp transition from  $S = 1$  to 0 around certain distance (e.g., the detectability of dwarf galaxies in flux-limited surveys, see §4.2), which can be approximated by a simple radial selection,

$$S(r | \alpha_i) = \begin{cases} 1, & r \in [r_{\text{obs,min}}, r_{\text{obs,max}}], \\ 0, & \text{otherwise,} \end{cases} \quad (9)$$

where  $[r_{\text{obs,min}}, r_{\text{obs,max}}]$  is the observable radial range of a given tracer. Note that this observable range depends on  $\alpha_i$ . The weight then becomes

$$\omega_i = \frac{1}{\int_{r_{\text{obs,min}}}^{r_{\text{obs,max}}} p(r | E_i, L_i) dr} = \frac{T_r[r_{\text{per}}, r_{\text{apo}}]}{T_r[r_{\text{obs,min}}, r_{\text{obs,max}}]} \Big|_{E_i, L_i}, \quad (10)$$

<sup>6</sup> If  $S \neq 0$  is guaranteed in the space of concern, a simpler alternative is  $\omega_i = 1/S(\mathbf{w}_i)$ , which is statistically equivalent to Eq. (7) for the whole sample.

<sup>7</sup> Eq. (8) assumed that the underlying dynamics (DF) is independent of the intrinsic properties  $\alpha$ ,  $f_{\Phi}(\mathbf{w} | \alpha) = f_{\Phi}(\mathbf{w})$ , which is a fairly general assumption for many tracer populations. When necessary, it is possible to extend  $\text{EMPDF}$  to the joint distribution of  $p(\mathbf{w}, \alpha)$ .

where  $T_r[a, b] \equiv 2 \int_{\max\{a, r_{\text{per}}\}}^{\min\{b, r_{\text{apo}}\}} dr / |v_r|$  is the time spent within the radius range for given orbit. The likelihood of Eq. (5) is rewritten as

$$p(\mathbf{w}_i | \Theta_{\Phi}, \alpha_i) = \frac{f_{\Phi}(\mathbf{w}_i)}{\int_{r_{\text{obs,min}}}^{r_{\text{obs,max}}} \varrho(r') 4\pi r'^2 dr'}, \quad (11)$$

where  $\varrho(r) = \int f_{\Phi}(E, L) 2\pi v^2 dv d \cos \vartheta$  is the tracer number density profile of the underlying sample with  $\cos \vartheta \equiv \hat{\mathbf{r}} \cdot \hat{\mathbf{v}} \in [-1, 1]$  and  $L = rv \sin \vartheta$ .

In practice, when selection function is involved, we suggest only using tracers more luminous than certain absolute magnitude threshold, thus excluding tracers with  $r_{\text{obs,max}}$  comparable to  $r_{\text{min}}$  of the sample (see §4.1 for example). Because such tracers will be assigned very high weights by Eq. (10), which may lead to nonrobust estimates dictated by a few high-weight tracers.

### 2.4 Treating observational errors

Another important observational effect is the measurement error. Intriguingly,  $\text{EMPDF}$  is robust against moderate observational errors even without any special treatment. As shown in §3.4 and Fig. 5, for hundreds of tracer with typical *Gaia* DR3 observational errors for satellite galaxies or globular clusters, the systematic bias in mass estimates introduced by these errors is much smaller than the statistical uncertainty and can thus be safely ignored. Therefore, it is not necessary to treat the observational errors explicitly for these tracers when inferring the MW mass.

However, more careful consideration might be necessary for tracers like halo stars due to their larger measurement errors and smaller statistical uncertainty given their large number. Overlooking observational errors may lead to artificial deviation from the steady state and biases in mass estimates. Similar to the selection function in §2.3, observational errors affect our method in two aspects: (a) construction of empirical DF and (b) likelihood under this DF.

(a) It is possible to derive the underlying “true” DF,  $f_{\Phi}(\mathbf{w})$ , by deconvolving the observational errors through a novel technique based on iterative reweighted importance sampling (IRIS) when performing the KDE in Eq. (2) (see Appendix C for details).

(b) The likelihood of an observed tracer  $\mathbf{w}_i$  (Eq. 5) can be obtained by marginalizing over the possible true  $\mathbf{w}_{\text{tr}}$  under the observational error  $p_{\text{err}}(\mathbf{w}_i | \mathbf{w}_{\text{tr}})$ .

$$p_{\text{ob}}(\mathbf{w}_i | \Theta_{\Phi}) = \int p_{\text{err}}(\mathbf{w}_i | \mathbf{w}_{\text{tr}}) f_{\Phi}(\mathbf{w}) d^6 \mathbf{w}_{\text{tr}}. \quad (12)$$

This can be computed efficiently using the Monte Carlo integration (see e.g., Li et al. 2020a, §3.2). We note that  $f_{\Phi}$  in above equation should be replaced with Eq. (11) when selection function is also involved.

A natural question might be why bother with deconvolving the observational scatter in step (a) if we will convolve it back in step (b). While these two procedures partially cancel each other out, they do not do so entirely. Nevertheless, this partial cancellation probably explains why this method is robust against moderate observational errors even without explicit correction.

## 3 METHOD VALIDATION AND COMPARISON

### 3.1 Mock tracer sample

We test our method using idealized mock samples and compare with several other methods. We consider halos that follow the spherical

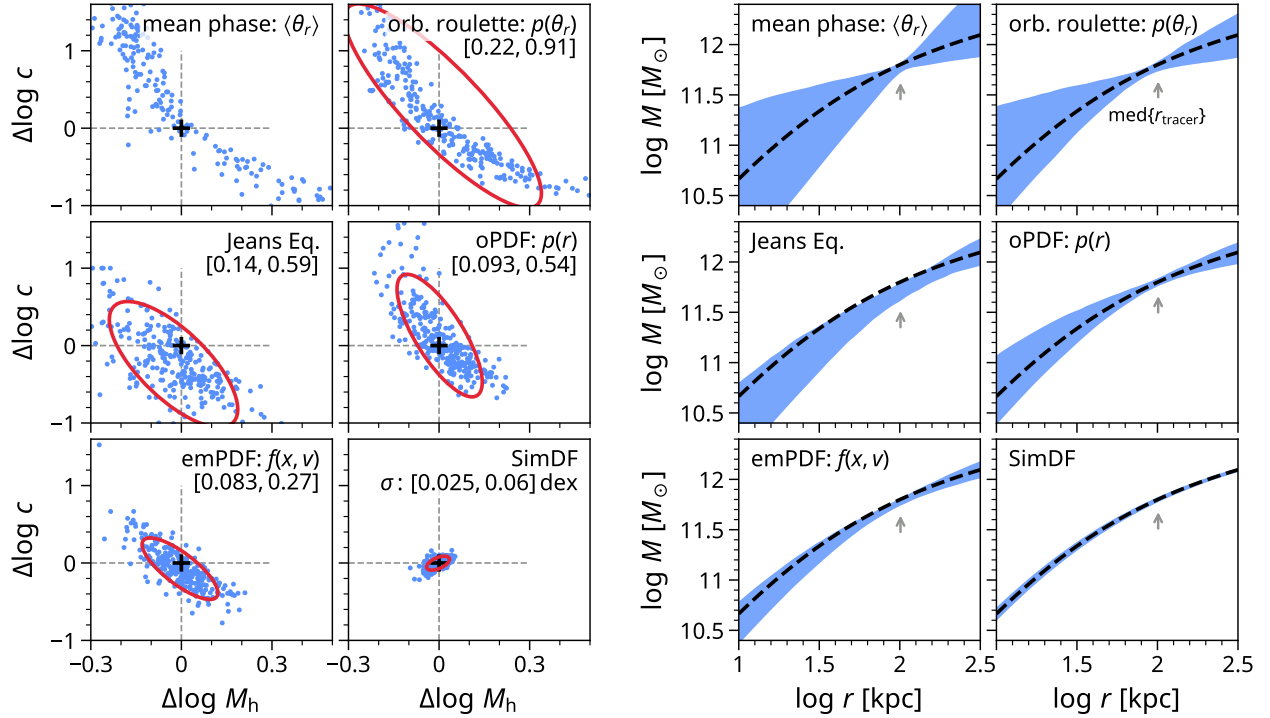


**Figure 3.** Method comparison based on idealized mock samples. Results are shown for 300 mock halos, each with 160 tracers, using six methods separately, mean phase, orbit roulette (Beloborodov & Levin 2004), spherical Jeans equation, oPDF (Han et al. 2016a), eMPDF (this work), and simulation-informed DF (Li et al. 2017, 2019). **Left panels:** Best-fit parameters (blue points) relative to their true values for individual mock halos. Each panel includes a  $1\sigma$  ellipse, indicating the mean and covariance of the points (not shown for “mean phase” with infinite inherent uncertainty). The root-mean-square error of  $\log M_h$  and  $\log c$  respective to their true values are provided in the upper-right corner of each panel. **Right panels:** 16th and 84th percentiles (blue shades) of the 300 best-fit mass profiles  $M(< r)$ . The black dashed curves show the true mass profile, and gray arrows indicate the median distance of tracers for reference. The simulation-informed DF shows the highest efficiency due to strong assumptions about tracer DFs but is limited to specific tracers like satellite galaxies. Among other methods for general tracers, eMPDF demonstrates optimal efficiency by fully exploiting the DF.

NFW density profile (Navarro et al. 1996), whose mass profile and potential are specified by the virial mass and concentration ( $M_h, c$ ),

$$\rho(r | M_h, c) = \frac{\rho_s}{(r/r_s)(1+r/r_s)^2}, \quad (13)$$

$$\Phi(r | M_h, c) = -4\pi G \rho_s r_s^2 \frac{\ln(1+r/r_s)}{r/r_s}, \quad (14)$$

where the characteristic density and radius,  $\rho_s$  and  $r_s$ , are determined by solving  $M_h = M(< R_h) = \frac{4\pi}{3} 200 \rho_{\text{crit}} R_h^3$  and  $R_h = cr_s$ . The target is to infer  $(M_h, c)$  from mock tracers.

We generate tracers for an NFW halo with  $M_h = 10^{12} M_\odot$  and concentration  $c = 10$ . For simplicity, we assume that the tracer spatial density follows the same profile as the host density (but with a squared-exponential truncation for  $r \gtrsim 500\text{kpc}$  for sampling efficiency) and the tracers have isotropic velocity anisotropy. Although this setup may not hold for MW tracers in reality, it does not affect the generality of our test. Following Li et al. (2023), the tracers are randomly sampled according to the theoretical DF using the Eddington (1916) formula and the AGAMA package (Vasiliev 2019)<sup>8</sup>. The tracers are guaranteed to be in steady state by construction. To mimic the MW halo tracers, we limit the mock observation to tracers in a radial range of [20, 300]kpc. We try different numbers of tracers  $N_{\text{tracer}}$  ranging from 10 to 2560 in a mock halo. For each  $N_{\text{tracer}}$ , we generate samples for 300 mock halos independently.

In this section, we aim to test the statistical efficiency of the method

with idealized mock samples and gain theoretical understanding. However, we note that the systematic errors due to the deviations from the model assumptions (steady state and spherical potential) are not involved in this test but can be important in practice. To estimate such systematics in future work, more realistic mocks can be taken from cosmological simulations (see e.g., Han et al. 2016b; Wang et al. 2017; Li et al. 2017, 2019, 2021; Wang et al. 2022b).

We apply the eMPDF method to the mock tracers and find the best-fit parameters  $(M_h, c)$  of the halo profile using Bayesian optimization. The parameters are searched within the range of  $11 < \log M_h/M_\odot < 13$  and  $-1 < \log c < 3$ .

### 3.2 Other methods for comparison

We compare the performance of eMPDF with five other methods, including mean phase, orbit roulette (Beloborodov & Levin 2004), oPDF (Han et al. 2016a), spherical Jeans equation, and simulation-informed DF (Li et al. 2017, 2019).

The first three methods share similar spirit as eMPDF, as mentioned in §1. We refer readers to Han et al. (2016a) for a summary and public implementation of these methods. Specifically, oPDF is based on binned statistics of the radial distribution of tracers. Through numerical experiments, we find that the optimal number of bins is approximately  $m = \max\{\ln(N), 2\}$ . Binning with equal counts slightly outperforms binning with equal widths. The result becomes insensitive to these details when  $N \gtrsim 200$ .

It is worth noting that the individual parameters are completely

<sup>8</sup> <https://github.com/GalacticDynamics-Oxford/Agama>

unconstrained by the mean phase method, except for their joint distribution. For each mock halo, there is not a unique best-fit point but rather a degeneracy curve in  $(M_h, c)$  space, as illustrated by Han et al. (2016a). The parameter search algorithm just returns a random single value along this degeneracy curve. The degeneracy leaves the mass profile unconstrained, except around the median tracer radius.

We also include the widely used spherical Jeans equation in the comparison. There are different ways to use the Jeans equation, ranging from purely data-driven to more parametric forms (also dubbed as “backward” and “forward” approaches, Rehehtulla et al. 2022). Here we adopt the backward form used by Li et al. (2021) without assuming parametric profiles for tracer density and anisotropy (see Appendix D for details). The Jeans equation demands a relatively large sample ( $N \gtrsim 100$ ) to ensure reasonable statistics, because it relies on the gradients of the tracer number density and velocity dispersion across adjacent radial bins.

It is interesting to compare with the simulation-informed DF (SimDF) method based on the scaling relation of satellite kinematics in cosmological simulations (Li et al. 2017, 2019), which has shown optimal statistical efficiency. This method assumes that the scaled orbital distribution,  $p(E/v_s^2, L/r_s v_s)$ , is universal across halos, as a natural generalization to the universal NFW density profile. Here  $v_s = r_s \sqrt{4\pi G \rho_s}$ , with  $r_s$  and  $\rho_s$  being the characteristic radius and density of the NFW profile. Extracting this distribution from simulations and combining it with the oPDF,  $p(r | E, L)$ , yields a steady-state template DF,  $f_0$ . The expected DF for a halo of arbitrary  $M_h$  and  $c$  is then given by the scaling relation

$$f(\mathbf{r}, \mathbf{v} | M_h, c) = r_s^{-3} v_s^{-3} f_0(\mathbf{r}/r_s, \mathbf{v}/v_s), \quad (15)$$

where  $(r_s, v_s)$  are the new characteristic scales determined by  $(M_h, c)$  (see an illustration in Fig. E1). In the original papers, the template DF  $f_0$  was constructed nonparametrically by rescaling and stacking satellites in cosmological simulations, following a similar procedure as described in §2.1. In this idealized test, we adopt the true halo DF as the template to mimic its performance. Clearly, unlike the other methods applicable to general tracers, the simulation-informed DF is limited to very specific tracers that are known to follow the scaling relation (e.g., satellite galaxies).

We refer interested readers to the literature (Han et al. 2016a,b; Wang et al. 2017, 2018; Li et al. 2019, 2021) for previous tests of these methods with idealized and realistic tracers.

### 3.3 Test results

The left panel of Fig. 3 presents the best-fit parameters inferred from six different methods for 300 mock halos, each with  $N_{\text{tracer}} = 160$  tracers. The right panel displays the corresponding best-fit profiles. In Fig. 4, we illustrate the root-mean-square error,  $\langle (x_{\text{best-fit}} - x_{\text{true}})^2 \rangle^{1/2}$ , of the best-fit  $\log M_h$  for 300 mock halos as a function of different  $N_{\text{tracer}}$ .

As expected, EMPDF provides the tightest constraints on both parameters among these methods (except for simulation-informed DF) due to its full exploitation of the DF. EMPDF yields an uncertainty in  $\log M_h$  that is smaller by factors of 2.5 and 1.5 compared to the phase roulette and Jeans equation methods, respectively (Fig. 4). While oPDF shows similar uncertainty in  $M_h$  as EMPDF, it exhibits a larger scatter in  $c$ , leading to a greater uncertainty in the inner halo mass profile (Fig. 3).  $M_h$  alone does not fully describe the mass profile, because the essential constraint is for the entire profile or equivalently the joint distribution of  $(M_h, c)$ .

As discussed in Han et al. (2016a), the spatial distribution used by

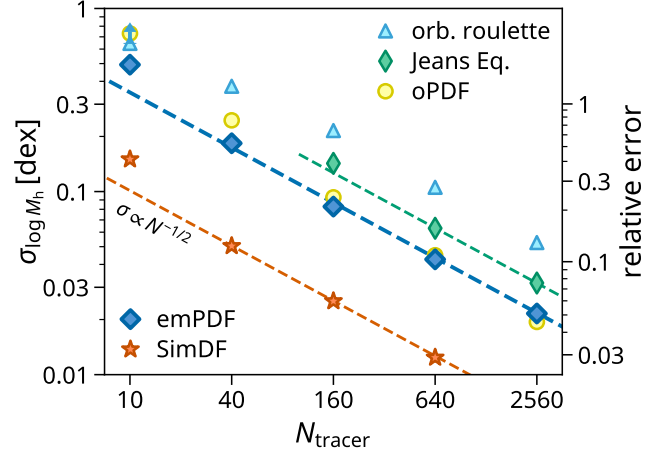


**Figure 4.** Performance as function of tracer number. The symbols show the root-mean-square error of the best-fit  $\log M_h$  of 300 mock halos with varying number of tracers. The dashed lines display  $\sigma \propto N^{-1/2}$  for reference. EMPDF gives smaller uncertainty than orbit roulette and Jeans equation by a factor of 2.5 and 1.5, respectively. oPDF shows similar uncertainty on  $M_h$  as EMPDF, but with a larger scatter in the concentration and inner density profile as shown in Fig. 3. The simulation-informed DF shows significantly smaller uncertainty owing to the additional model assumption.

oPDF contains more information than the simple mean phase estimator or the phase angle distribution (orbit roulette). The difference also partly arises because the maximum likelihood estimator employed by oPDF is more efficient than the minimum distance estimator by orbital roulette. While EMPDF shows better constraints, especially on  $c$ , than oPDF for  $N_{\text{tracer}} \lesssim 1000$ , we find that their performance becomes similar for larger  $N$ . This suggests that EMPDF does not gain much additional information from velocity components beyond the spatial distribution. This may not be surprising, considering that the position determines velocity in a given orbit and that the density profile largely determines the DF when the velocity anisotropy is known (implicitly provided here by the tracer sample). At low  $N_{\text{tracer}}$ , the better performance of EMPDF largely benefits from smoothing compared to binned statistics in oPDF, which becomes less significant with large samples. Nevertheless, besides its better performance for small samples, the complete DF provided by EMPDF is useful as a complete description of tracer kinematics.

The Jeans equation demonstrates inferior efficiency compared to EMPDF, as it uses only the first and second moments of the DF, thereby losing information in high-order moments. In Fig. 3, a mild bias is observed in the estimates from the Jeans equation, likely due to limited binned statistics given the relatively small sample size. We confirm that this bias diminishes with larger samples (also cf. Li et al. 2021, where a greater number of tracers was used).

Interestingly, except for the simulation-informed DF method, all methods show a similar “sweet point” around the median radius of the tracers, where the mass profile is best constrained with minimal uncertainty. This optimal constraint radius has been reported for various methods (see Han et al. 2016a for discussion) and has motivated the development of so-called Jeans estimators (e.g., Walker et al. 2009; Wolf et al. 2010). The uncertainty at the sweet point is similar for the four minimal assumption methods (mean phase, orbital roulette, oPDF, and EMPDF), indicating a limit to the information that can be gained. This behavior explains the similar degeneracy in the inferred  $(M, c)$  seen in the left panel of Fig. 3. Nonetheless, the EMPDF method provides significantly better constraints on the overall density profile.

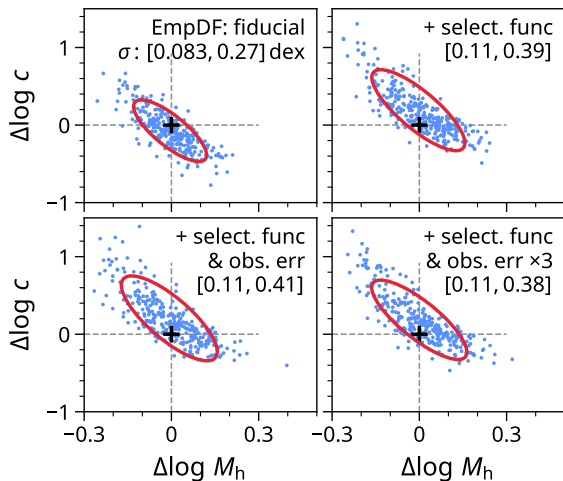


**Figure 5.** Similar to Fig. 3 left panels, but showing EMPDF results for mock tracers with selection function and observational errors. **Upper left:** Fiducial samples without any observational effects, identical to the left panel of Fig. 3. **Upper right:** Mocks with selection function. **Lower left:** Mocks with selection function and observational errors, mimicking the *Gaia* DR3 precision for MW satellites and globular clusters. **Lower right:** Same as previous, but with the observational errors tripled. We exert the selection function correction described in §2.3 when applicable, but without any explicit treatment for observational error in this test.

The simulation-informed DF method shows the highest efficiency, significantly surpassing the other five methods, due to the strong assumption about the form of the DF and a coupling between DF and potential through scaling relations. With this particular assumption, we may expect its efficiency to be even higher than typical analytical DF models. However, the simulation-informed DF is limited to very specific tracers, as mentioned above, placing it in a different category. The EMPDF method has the theoretically optimal efficiency for general tracers with minimal model assumptions.

### 3.4 Tests with selection function and observational error

We test the validity of EMPDF for tracers with observational effects. As detailed in Appendix F, we generate mock data with a selection function and observational errors to mimic typical *Gaia* DR3 observations for MW dwarf satellites, where completeness and observational errors depend on the apparent magnitude of the tracers.

We generate 300 mock halos, each with  $N_{\text{tracer}} = 160$  tracers within  $[20, 300]$  kpc. This sample size is higher than the actual number of available MW satellites, so any systematics will be more appreciable due to the reduced statistical error. We apply the selection function treatment described in §2.3, but do *not* apply any explicit treatment for observational error. For reference, we also provide a fiducial mock sample with the same  $N_{\text{tracer}}$  and radial range, but without the observational effects.

The results are shown in Fig. 5, which generally justifies our correction for the selection function in §2.3. Compared to the fiducial case, the uncertainty with incomplete data is slightly larger. This increase is because of the reduced median distance of observed tracers, weakening constraints on the virial scale, and the reduced effective tracer number due to unequal correction weights during the DF construction (see Eq. 10). A slight bias appears in  $c$ , possibly also related to uneven correction weights. We leave possible technical improvements to future works.

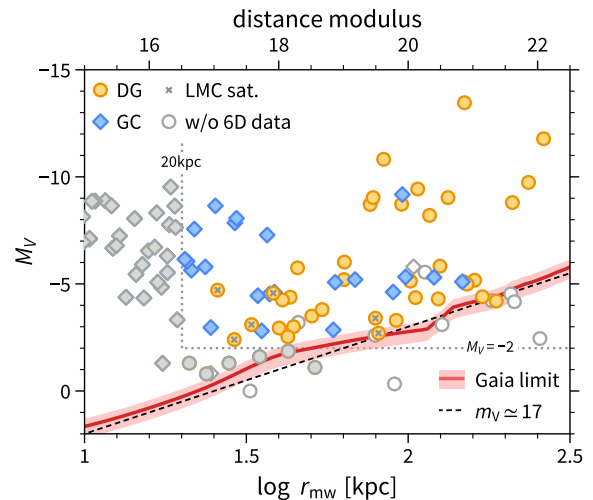


**Figure 6.** Galactocentric distance and absolute magnitude of MW tracers, including dwarf galaxies (DGs) and globular clusters (GCs). We select the tracers brighter than  $M_V = -2$  within  $[20, 300]$  kpc, as indicated by the dotted lines, tracers outside of which are shown in gray. Tracers without reasonable 6D kinematic measurements (open symbols) and possible LMC satellites (crosses) are excluded. The red solid curve shows the completeness distance  $r_{\text{obs,max}}(M_V)$  for *Gaia* limits, effectively distinguishing tracers with valid kinematic data from those without. For reference, the black dashed line indicates a constant apparent magnitude of  $m_V = 17$ . Low-luminosity tracers are clearly incomplete at large distances. Thus, observed tracers represent a larger underlying sample. Correcting for selection function is crucial for unbiased dynamical modeling.

Unmodeled observational errors may introduce systematic error into the inference in theory. However, in Fig. 5, EMPDF yields nearly identical results for mocks without and with observational errors, even when the observational errors are tripled. Clearly, this systematic error is much smaller than the statistical error for  $N_{\text{tracer}} = 160$  (or smaller  $N_{\text{tracer}}$ ), and thus can be safely ignored without explicit treatment. The insensitivity to moderate observational error is noteworthy. As discussed in §2.4, it is likely because both the instantaneous kinematics and the empirical DF are changed by observational errors in a similar way. Therefore, we do not apply any correction for observational errors in the next section, where satellite galaxies and globular clusters are used as MW tracers.

Further tests indicate that systematic error due to unmodeled observational uncertainties becomes appreciable only for substantially larger tracer number (reduced statistical error) or observational error (increased bias). In such cases, explicit modeling of observational error (see §2.4) is necessary.

## 4 APPLYING TO THE MILKY WAY

We aim to measure the Milky Way (MW) mass profile using EMPDF. We assume the MW total mass distribution (including baryonic contribution) to be a spherical NFW profile, characterized by virial mass and concentration,  $M_{200c}$  and  $c$ . Hydrodynamical cosmological simulations show that the total mass profile of MW-sized halos can be well approximated by the NFW profile for  $r > 0.05R_{\text{vir}}$  ( $\sim 10$  kpc for MW) (e.g., EAGLE, Schaller et al. 2015). Though the inner halo is affected by the stellar disk, using a spherical potential for the outer halo is probably justifiable, especially recalling that the potential is always more spherical than the density distribution (BT08). In the



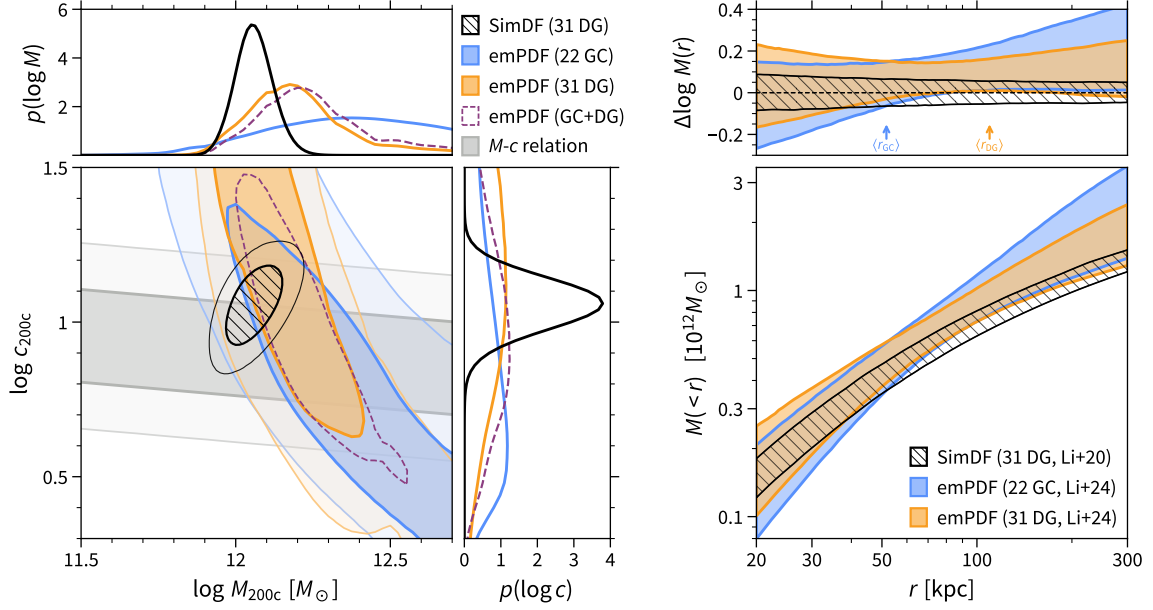


**Figure 7.** **Left:** MW halo mass and concentration inferred by emPDF using *Gaia* DR3 kinematics of DGs or/and GCs. The contours represent the  $1\sigma$  (68.3%) and  $2\sigma$  (95.4%) regions for different constraints (see legend), where flat priors for  $\log M_{200c}/M_{\odot} \in [11.5, 12.7]$  and  $\log c_{200c} \in [0.3, 1.5]$  are used. For clarity, only the  $1\sigma$  contour is shown for combined constraints with DGs and GCs. An updated estimate using DGs and the simulation-informed DF (Li et al. 2020a) is also shown for comparison. Marginalized distributions are displayed in the upper and right subpanels. The  $M$ - $c$  relation is shown in gray for reference but *not* used. **Right:** 16th and 84th percentiles of best-fit MW profiles. The residuals relative to the best fit of the simulation-informed DF are shown in the upper subpanel. emPDF constraints with DGs and GCs exhibit slightly different degeneracy directions due to distinct spatial distributions, as indicated by their median radii (shown as arrows). The various constraints agree within  $1\sigma$ .

future, more flexible profiles can be considered (e.g., Cautun et al. 2020; Dekel et al. 2017; Freundlich et al. 2020) with additional stellar components. Here we limit our analysis to the radial range  $r \in [20, 300]$  kpc.

#### 4.1 Observation data

In this work, we utilize the latest kinematic data of the MW tracers from *Gaia* DR3 (2023) and complementary spectroscopic observations, including faint satellite dwarf galaxies (DGs, exclusive of the Magellanic Clouds, LMC and SMC) from Pace et al. (2022, with “fixed” background model)<sup>9</sup>, and globular clusters (GCs) from Vasiliev & Baumgardt (2021)<sup>10</sup>. The properties used in our analysis include the  $V$ -band magnitude, sky coordinates ( $\alpha, \delta$ ), distances to the sun ( $d_{\odot}$ ), line-of-sight velocities ( $v_{\text{los}}$ ), and proper motions ( $\mu_{\alpha}^*, \mu_{\delta}$ ). Following Li et al. (2020a), the kinematics are transformed from Heliocentric frame into Galactocentric frame (Bland-Hawthorn & Gerhard 2016). We convert the apparent  $V$ -magnitude  $m_V$  to absolute magnitude via  $M_V = m_V - 5 \log(d_{\odot}/\text{kpc}) - 10$ .

Out of the 54 DGs and 165 GCs in the parent sample, we have 53 and 24 objects in the radial range  $r \in [20, 300]$  kpc. We exclude tracers without line-of-sight velocity measurements or with large mean proper motion uncertainties  $\bar{\epsilon}_{\mu} = (\epsilon_{\mu_{\alpha}^*} + \epsilon_{\mu_{\delta}})/2 > 0.2 \text{ mas/yr}$ , which results in 43 DGs and 22 GCs. We further exclude the six DGs likely associated with LMC: Car II, Car III, Hor I, Hyi I, Phx II, and Ret II (Pardy et al. 2020; Pace et al. 2022) to avoid potential bias. We also exclude tracers fainter than  $M_V = -2$  whose completeness is relatively less understood, leaving 31 DGs and 22 GCs in the final

sample.<sup>11</sup> The parent dataset and the subsample used in our analysis are shown in Fig. 6.

#### 4.2 Selection function

Clearly, faint tracers at large distance are largely missed in the lower-right corner in Fig. 6. To prevent the bias introduced by incompleteness (cf. discussion in Li et al. 2020a), we should either limit ourselves to volume limited subsample or take the selection function into consideration as described in §2.3. As the DGs and GCs were discovered by multiple sky surveys with different depths, the selection function is a complicated function of both distance and sky coordinates. Fortunately, requiring *Gaia* DR3 measurements further posed a uniform selection on the parent sample (assuming those surveys are deeper than *Gaia*), which simplifies the task.

We find a good approximate selection function for these tracers with *Gaia* DR3 kinematics following Li et al. (2020a). Assuming that *Gaia* can measure the proper motion of a DG/GC reliably only when it contains at least  $\sim 5$  member stars brighter than the limit  $m_{V,\text{star}} \sim 21$  (Gaia Collaboration et al. 2023), we can derive the maximum observable radius  $r_{\text{obs,max}}(M_V)$  as a function of the luminosity, using synthetic member stars generated by the PARSEC stellar model library (Bressan et al. 2012)<sup>12</sup> for a typical stellar population with a Chabrier (2001) mass function, an age of 12.5 Gyr,

<sup>11</sup> Such faint satellites represent a largely unobserved parent sample, thus assigned high incompleteness correction weights in emPDF. Any uncertainty in completeness correction will be amplified. Moreover, extremely unequal weights reduce the effective tracer number, also leading to inferior inference. The latter effect can possibly be mitigated by using weight-dependent smoothing kernel when constructing empirical DF in the future.

<sup>12</sup> [http://stev.oapd.inaf.it/cgi-bin/cmd\\_3.7](http://stev.oapd.inaf.it/cgi-bin/cmd_3.7). We queried the

<sup>9</sup> <https://zenodo.org/record/7158669>

<sup>10</sup> <https://people.smp.uq.edu.au/HolgerBaumgardt/globular>

and a metallicity of  $[\text{Fe}/\text{H}] = -2.2$ . As shown by the red solid curve in Fig. 6, this  $r_{\text{obs,max}}(M_V)$  distinguishes the tracers with and without valid kinematic data very well, suggesting a sharp transition in completeness,<sup>13</sup> thus justifying the use of Eq. (9). The shaded band around this curve corresponds to  $N(m_{V,\text{star}} < 21) = 5 \pm 2$  for reference. At the luminous end, the above curve is close to a total magnitude cut of  $m_V = 17$ , which happens nearly identical to the detection limit of DGs for SDSS survey (Walsh et al. 2009).

In addition to the selection on distance, the spatial distribution of satellites is further truncated by the angular coverage of the sky surveys and partly blocked by foreground dust and stellar light of the disk. However, as pointed out in Li et al. 2020a, this angular selection does not affect our analysis when assuming a spherical DF.

We note that the above *Gaia*-based selection function is somewhat empirical. We refer the interested readers to the general reviews of DG and GC populations (Simon 2019; Gratton et al. 2019) and dedicated discussions on completeness of DGs (Koposov et al. 2008; Walsh et al. 2009; Jethwa et al. 2016; Nadler et al. 2020; Manwadkar & Kravtsov 2022) and GCs (Webb & Carlberg 2021).

Finally, we reiterate that a rigorous and straightforward treatment of the selection function is an important virtue of the DF methods, including EMPDF. This approach allows for full exploitation of the available observational data. In contrast, dynamical methods relying on a volume-limited complete sample must either remove abundant faint tracers or limit the analysis to a small volume.

### 4.3 Constraining the MW potential

We apply the EMPDF method to DGs and GCs separately. For each tracer labeled  $i$ , we consider the selection function (§4.2) with a maximum observable radius  $\max\{r_{\text{obs,max}}(M_{V,i}), r_i\}$  individually. The correction for the selection function (described in §2.3) is used, but without explicit treatment for observational errors (justified in §3.4). The likelihood is estimated on a dense 2D grid of  $(\log M_{200c}, \log c)$  for  $\log M_{200c}/M_\odot \in [11.5, 12.7]$  and  $\log c \in [0.3, 1.5]$  with *flat priors*. This range of  $c$  covers the  $4\sigma$  region of the  $M$ - $c$  relation for this mass range in hydrodynamical simulations (Schaller et al. 2015). Flat priors are used to avoid relying on extra information. The confidence regions and the marginalized distributions of parameters are estimated from the posterior on the grid.

The likelihood contours of the inferred parameters are shown in the left panel of Fig. 7. The corresponding mass profiles are displayed in the right panel. These parameters and mass profiles are also provided in Table 1. Similar to Fig. 3, a strong degeneracy between  $M$  and  $c$  is observed, corresponding to the most constrained “sweet point” in the mass profile near the mean tracer radius.<sup>14</sup> The inferences with DGs and GCs are mutually consistent. DGs provide better constraints than GCs for  $r > 60\text{kpc}$ , owing to their larger sample size and more extended spatial distribution. We also present joint constraints from DGs and GCs by multiplying their likelihoods, which results in tighter overall constraints.

We emphasize that the constrained mass profile is more fundamental than the inferred virial mass. The virial mass is merely one

synthetic samples in batch using a script written by Zhaozhou Li (as part of Li et al. 2020b), [https://github.com/syrte/query\\_isochrone](https://github.com/syrte/query_isochrone).

<sup>13</sup> In principle, we should use Heliocentric distance rather than the Galactocentric  $r$ . Nevertheless the resulted difference in enclosed volume is small as  $r_{\text{obs,max}}$  is far beyond the solar location.

<sup>14</sup> In contrast to Fig. 3, here the best-constrained radius is not exactly at the median tracer radius due to selection function correction.

**Table 1.** MW mass profile inferred from dwarf galaxies (DGs) and globular clusters (GCs) with EMPDF and simulated-based DF (SimDF).

Method	EMPDF	EMPDF	EMPDF	SimDF
Tracer	GC	DG	GC+DG	DG
$N_{\text{tracer}}$	22	31	53	31
$r_{\text{med}}$	36.0	101.6	68.5	101.6
$r_{\text{avg}}$	51.7	109.7	85.6	109.7
$M(<20\text{kpc})$	$0.12^{+0.08}_{-0.04}$	$0.17^{+0.08}_{-0.07}$	$0.15^{+0.07}_{-0.05}$	$0.15^{+0.03}_{-0.03}$
25	$0.17^{+0.10}_{-0.05}$	$0.23^{+0.09}_{-0.08}$	$0.20^{+0.08}_{-0.06}$	$0.20^{+0.04}_{-0.03}$
30	$0.22^{+0.11}_{-0.06}$	$0.28^{+0.09}_{-0.09}$	$0.26^{+0.08}_{-0.07}$	$0.24^{+0.05}_{-0.04}$
40	$0.32^{+0.13}_{-0.07}$	$0.39^{+0.09}_{-0.10}$	$0.36^{+0.08}_{-0.08}$	$0.33^{+0.06}_{-0.05}$
50	$0.43^{+0.14}_{-0.08}$	$0.48^{+0.10}_{-0.10}$	$0.46^{+0.08}_{-0.07}$	$0.41^{+0.07}_{-0.06}$
65	$0.58^{+0.17}_{-0.09}$	$0.61^{+0.10}_{-0.11}$	$0.60^{+0.08}_{-0.07}$	$0.51^{+0.08}_{-0.07}$
80	$0.74^{+0.18}_{-0.14}$	$0.73^{+0.12}_{-0.12}$	$0.74^{+0.09}_{-0.09}$	$0.60^{+0.09}_{-0.07}$
100	$0.95^{+0.23}_{-0.22}$	$0.87^{+0.15}_{-0.15}$	$0.90^{+0.13}_{-0.13}$	$0.71^{+0.10}_{-0.08}$
125	$1.19^{+0.30}_{-0.33}$	$1.03^{+0.20}_{-0.18}$	$1.07^{+0.21}_{-0.18}$	$0.83^{+0.11}_{-0.09}$
160	$1.48^{+0.46}_{-0.48}$	$1.21^{+0.29}_{-0.24}$	$1.29^{+0.32}_{-0.25}$	$0.97^{+0.12}_{-0.10}$
200	$1.78^{+0.66}_{-0.64}$	$1.39^{+0.41}_{-0.30}$	$1.49^{+0.46}_{-0.34}$	$1.10^{+0.14}_{-0.12}$
250	$2.10^{+0.93}_{-0.83}$	$1.55^{+0.57}_{-0.35}$	$1.70^{+0.63}_{-0.40}$	$1.24^{+0.16}_{-0.13}$
320	$2.46^{+1.29}_{-1.03}$	$1.77^{+0.73}_{-0.45}$	$1.95^{+0.84}_{-0.51}$	$1.39^{+0.17}_{-0.14}$
400	$2.81^{+1.69}_{-1.24}$	$1.96^{+0.92}_{-0.51}$	$2.18^{+1.08}_{-0.62}$	$1.53^{+0.19}_{-0.15}$
$M_{200c}$	$3.67^{+0.73}_{-2.26}$	$1.68^{+0.34}_{-0.62}$	$1.68^{+0.69}_{-0.55}$	$1.14^{+0.16}_{-0.14}$
$R_{200c}$	$318^{+20}_{-87}$	$245^{+16}_{-35}$	$245^{+30}_{-31}$	$215^{+10}_{-9}$
$c_{200c}$	$3.0^{+8.4}_{-0.5}$	$10.0^{+20.2}_{-3.1}$	$9.1^{+8.9}_{-4.8}$	$11.5^{+2.3}_{-1.9}$
$\log M_{200c}$	$12.42 \pm 0.33$	$12.16 \pm 0.16$	$12.23 \pm 0.16$	$12.06 \pm 0.06$
$\log c_{200c}$	$0.71 \pm 0.47$	$1.12 \pm 0.37$	$0.98 \pm 0.29$	$1.06 \pm 0.08$
$\rho_{\text{corr}}$	-0.89	-0.80	-0.86	0.55

Rows. Type, number, median and mean Galactocentric distances [kpc] of tracers; MW mass within a series of radii,  $M(<r)[10^{12}M_\odot]$ ; inferred virial mass, radius, and concentration,  $M_{200c}[10^{12}M_\odot]$ ,  $R_{200c}[\text{kpc}]$ ,  $c_{200c}$ ; 2D Gaussian fitting to the joint distribution of  $\log(M_{200c}/M_\odot)$  and  $\log c_{200c}$ , including mean  $\pm$  standard deviation and correlation coefficient  $\rho_{\text{corr}}$ .

Notes. (a) The estimated masses are for the total mass, including baryons. (b) The uncertainties are for 16% and 84% percentiles ( $1\sigma$ ). (c) We emphasize that the constrained mass profile is more fundamental than the fitting parameters. Merely quoting the inferred halo mass can be meaningless when the  $M$ - $c$  degeneracy is strong.

of the parameters and does not fully describe the mass profile alone. Its value may have large uncertainty and even bias if the virial radius extends far beyond the tracer sample (cf. Li et al. 2020a, fig. 9). The extrapolation becomes unreliable because it depends on an assumed functional form of the profile, which may not be suitable for the full radial range. However, over the radial range covered by tracers, the mass profile remains well constrained. For example, one might think that MW virial mass by GCs is significantly overestimated with unrealistic concentration according to the left panel of Fig. 7, but upon examining the right panel, this profile is actually reasonably constrained.

For comparison, we also show an updated constraint by the simulation-informed DF using scaling relations of satellite kinematics in the EAGLE simulation (Li et al. 2019, 2020a) in Fig. 7. The

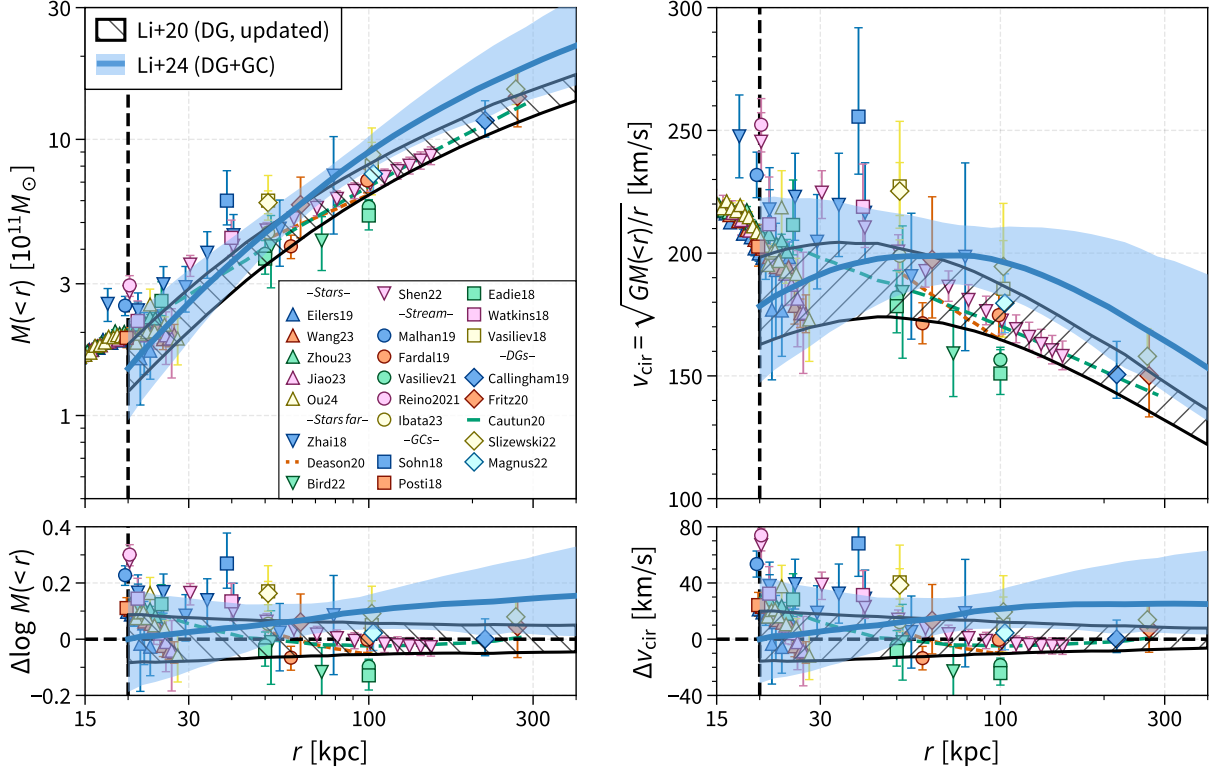


**Figure 8.** Comparison of the inferred MW mass profile (left) and rotation curve (right). Shown are our new estimates based on GC+DGs (blue curves with  $1\sigma$  error bands) and the updated estimate of Li et al. (2020a) based on DGs (striped  $1\sigma$  error bands). Other symbols or lines represent recent measurements since 2018 using various tracers, including stars within 30 kpc (Eilers et al. 2019; Wang et al. 2023; Zhou et al. 2023; Jiao et al. 2023; Ou et al. 2024), more distant halo stars (Zhai et al. 2018; Deason et al. 2021; Bird et al. 2022; Shen et al. 2022; Shen et al. 2022), stellar streams (Malhan & Ibata 2019; Fardal et al. 2019; Vasiliev et al. 2021; Reino et al. 2021; Ibata et al. 2024), GCs (Sohn et al. 2018; Posti & Helmi 2019; Eadie et al. 2018; Watkins et al. 2019; Vasiliev 2018), and DGs (Callingham et al. 2019; Cautun et al. 2020; Fritz et al. 2020; Slizewski et al. 2022; Correa Magnus & Vasiliev 2022). Studies that used multiple tracer populations are categorized by the most distant tracers. Small offsets in  $r$  are added to reduce overlap. Most recent estimates of the MW mass profile are consistent within  $\pm 0.15$  dex.

original estimates by Li et al. (2020a) were made for a similar DG sample with *Gaia* DR2 data (Gaia Collaboration et al. 2018), but for  $r \in [40, 300]$  kpc. Using the same simulation-informed DF model and a flat prior, we update the constraints using the updated DG sample with *Gaia* DR3 kinematics and corresponding selection function presented in this paper. The updated parameters are very close to those originally reported by Li et al. (2020a,  $M_{200c} = 1.29^{+0.24}_{-0.20} M_{\odot}$  and  $c = 11.0^{+4.8}_{-3.3}$ ), but with reduced uncertainty of concentration due to additional tracers used for  $r < 40$  kpc.

While consistent with the results of EMPDF within  $1\sigma$ , the simulation-informed DF provides much tighter constraints. This improvement benefits from additional knowledge learnt from simulation on orbital distribution and its scaling relation with potential, as discussed in §3.3. In contrast, the EMPDF method constructs the orbital distribution from observed tracers. This difference also leads to a different parameter degeneracy direction. As shown in the right panel, the inferred profile by simulation-informed DF does not exhibit a “sweet point”, but shows a rather uniform uncertainty that is only slightly larger inward. This demonstrates the advantage of the simulation-informed method, despite at the cost of dependence on simulations. Nevertheless, EMPDF with the same DG sample shows similar uncertainties as simulation-informed DF around the median tracer radius.

We also show the mass-concentration ( $M$ - $c$ ) relation in cosmological hydrodynamical simulations in Fig. 7 for reference. Shown

in the median relation,  $\log c = 0.912 - 0.087 \log(M_{200c}/10^{12} M_{\odot})$  (Schaller et al. 2015, EAGLE simulation), with a scatter of 0.15 dex (Jing 2000). This relation is only slightly different from that in dark-matter-only simulations. All the constraints above overlap with this relation.

#### 4.4 Comparison with previous work

There is a considerable effort devoted to the MW mass estimates, based on different tracer populations and methods. We refer readers to Wang et al. 2020 for a comprehensive review (also Bobylev & Baykova 2023 for a recent compilation). Below we list some recent work (not exhaustive) in several categories.

- Stars of the inner halo with 30 kpc (Eilers et al. 2019; Ablimit et al. 2020; Wang et al. 2023; Zhou et al. 2023; Jiao et al. 2023; Ou et al. 2024) and more distant halos stars (Xue et al. 2008; Huang et al. 2016; Ablimit & Zhao 2017; Zhai et al. 2018; Deason et al. 2021; Bird et al. 2022; Shen et al. 2022). Most studies use the Jeans equation, while some employ DF models (Deason et al. 2021; Shen et al. 2022).
- Stellar streams (Gibbons et al. 2014; Malhan & Ibata 2019; Fardal et al. 2019; Reino et al. 2021; Vasiliev et al. 2021; Ibata et al. 2024).
- Globular clusters (Sohn et al. 2018; Posti & Helmi 2019; Eadie et al. 2018; Watkins et al. 2019; Vasiliev 2018; Wang et al. 2022a)

and satellite galaxies (Boylan-Kolchin et al. 2013; Patel et al. 2018; Callingham et al. 2019; Cautun et al. 2020; Li et al. 2020a; Fritz et al. 2020; Slizewski et al. 2022; Correa Magnus & Vasiliev 2022; Kravtsov & Winney 2024). Jeans mass estimators are widely used due to the limited tracer sample size. Some studies utilize DF models as well (Li et al. 2017, 2020a; Eadie et al. 2018; Callingham et al. 2019; Wang et al. 2022a).

- Escape velocity of stars (Smith et al. 2007; Deason et al. 2019; Grand et al. 2019; Necib & Lin 2022; Roche et al. 2024).
- Dynamics of the Local Group (Li & White 2008; Boylan-Kolchin et al. 2013; Peñarrubia et al. 2016; Peñarrubia & Fattahi 2017; Li & Han 2021).

In Fig. 8, we compare our new measurements with selected recent literature after 2018, most of which utilize proper motion measurements by HST or Gaia. We display the mass profile and its alternative expression in terms of the rotation curve  $v_{\text{cir}} = \sqrt{GM(<r)}/r$ . Most recent estimates of the MW mass profile are consistent within  $\pm 0.15$  dex. The estimates by EMPDF appear slightly higher than the other measurements, but this deviation is not very significant given the uncertainty band.

It is noted that the MW masses inferred by EMPDF and simulation-informed DF show a trend lower than estimates by stars for  $r \lesssim 20$  kpc and likely more so inwards. This discrepancy arises because a single NFW profile cannot adequately describe the additional stellar components within this radius, prompting us to limit our analysis to  $r > 20$  kpc. Future work may address this issue by using a more flexible model with multiple components for the MW mass profile.

Many studies also provide estimates of the MW virial mass. We reiterate that it is more meaningful to compare inferred density profiles in regions directly constrained by tracers. Extrapolation is unreliable, especially when inferring virial mass from tracers located in the very inner halo, which is highly sensitive to the assumed functional form for mass profiles. A workaround involves combining multiple tracer populations to obtain better constraints on a full radial range (e.g., McMillan 2017; Cautun et al. 2020; Karukes et al. 2019; Li et al. 2020a).

## 5 DISCUSSION: EXTENSIONS OF THE METHOD

Han et al. (2016a) discussed various extensions to the OPDF method and its connections to other methods, including analytical DFs (Wang et al. 2015b; Han et al. 2016b), the Schwarzschild (1979) method, and the orbital roulette (Beloborodov & Levin 2004). Most of these discussions apply to EMPDF as an upgrade to the OPDF method. We briefly discuss some of them below.

The EMPDF method can be extended to axisymmetric or triaxial systems by using the actions  $\mathbf{J}$  instead of  $(E, L)$  to characterize the orbital distribution. When such calculations are difficult, direct numerical integration of the orbits can be used to obtain the time-averaged 6D distribution in a way similar to the Schwarzschild method. Following the phase-mark method in Han et al. (2016a), it is possible to apply EMPDF to separate radial bins to obtain local potential estimates and reconstruct the entire potential profile non-parametrically from these segmented estimates. When some dimensions of tracer kinematics are lacking in observation, the missing information may be recovered statistically based on the symmetry of the system (Dehnen & Binney 1998; Wegg et al. 2019) or treated as observations with extremely large errors (cf. §2.4).

In what follows, we provide more extended discussions on EMPDF

expressed in action space and its connection to the minimum entropy principle.

### 5.1 EMPDF in action space and minimum entropy

In this work we used  $p(E, L)$  to characterize the orbital distribution. One can use combinations of other orbital integrals as well, such as circular radius and orbital circularity ( $r_{\text{cir}}, \epsilon$ ), or actions  $\mathbf{J}$ . A particular interest in actions is that  $\mathbf{J}$  and their conjugated angles,  $\boldsymbol{\theta}$ , are the so-called canonical coordinates (BT08, sec. 3.5) such that  $f(\mathbf{r}, \mathbf{v}) = p(\mathbf{J}, \boldsymbol{\theta}) = (2\pi)^{-3} p(\mathbf{J})$  with unity Jacobian. Similar to  $p(E, L)$ , the orbital distribution  $p(\mathbf{J})$  can be constructed empirically from the tracer sample  $\{\mathbf{J}_i\}$  using KDE.<sup>15</sup>

The log-likelihood between the empirical DF and observation (Eq. 6, without prior) is rewritten as

$$\ln \mathcal{L} = \sum_{i=1}^N \ln f(\mathbf{w}_i) = \sum_{i=1}^N \ln p(\mathbf{J}_i) - 3N \ln(2\pi) \quad (16)$$

This is the *same* likelihood, just in a different form. On the other hand, the entropy of the action distribution of the sample is

$$H = -\int p(\mathbf{J}) \ln p(\mathbf{J}) d^3 \mathbf{J} \simeq -\frac{1}{N} \sum_{i=1}^N \ln p(\mathbf{J}_i) \quad (17)$$

Therefore, maximizing the EMPDF likelihood is equivalent to *minimizing the entropy* of actions or *maximizing their clustering* (recall that a flat distribution has maximum entropy). Note that this correspondence to entropy arises only when  $p(\mathbf{J})$  is constructed directly from the sample  $\{\mathbf{J}_i\}$  itself, and it thus does not hold for general dynamical modeling methods other than EMPDF.

Beraldo e Silva et al. (2024) recently proposed a dynamical modeling method based on minimum entropy in action space, bearing the same mathematical expression as above. We argue that EMPDF represents a more fundamental framework, where the minimum entropy principle can be derived as a phenomenological result as shown above. The concept of EMPDF theoretically justifies why we should minimize the entropy of actions to infer the potential, rather than the entropy of other coordinates such as  $(\mathbf{r}, \mathbf{v})$  or  $(E, L)$ . Essentially, EMPDF seeks the minimum difference (KL-divergence) between the time-averaged distribution,  $f(\mathbf{r}, \mathbf{v})$ , and the instantaneous observed kinematics,  $\{\mathbf{r}_i, \mathbf{v}_i\}$ , which involves two distributions rather than a single distribution. Though the KL-divergence has the similar form as entropy when the two distributions are both expressed in terms of actions,  $f(\mathbf{J}) = (2\pi)^{-3} p(\mathbf{J})$  and  $\{\mathbf{J}_i\}$ , they hold different meanings nevertheless. The perspective of EMPDF also allows for a more natural treatment of observational effects.

Despite the different contexts and physical motivations, it is also intriguing to note the resemblance between EMPDF and the clustering-based inference with stellar streams. The latter searches for the best-fit Galactic potential by maximizing the clustering of stream member stars in action space (Helmi & White 1999; Sanderson et al. 2015; Buckley et al. 2019; Yang et al. 2020; Reino et al. 2021, also cf. Peñarrubia et al. 2012; Brooks et al. 2024 in energy space).

<sup>15</sup> In spherical symmetry, one can choose the actions  $(J_r, L, L_z)$ , where  $L_z \equiv \mathbf{L} \cdot \mathbf{e}_z$  follows a uniform distribution in  $[-L, L]$ . The KDE procedure thus becomes simpler with  $p(J_r, L, L_z) = \frac{1}{2L} p(J_r, L)$ . Also note that the transformation to action-angle coordinates is feasible only if the potential is integrable and not dominated by resonances or chaotic regions (see e.g., BT08, Price-Whelan et al. 2021). This condition is typically met for many simple potential models.

## 6 CONCLUSIONS

We propose the  $\text{EMPDF}$ , a novel dynamical modeling method for general tracers with the optimal statistical efficiency under the minimal assumption of steady state.  $\text{EMPDF}$  searches for the best-fit potential by maximizing the similarity between instantaneous kinematics and the time-averaged DF. This DF is empirically constructed from observation upon the theoretical foundation of  $\text{oPDF}$  (Han et al. 2016a), thereby eliminating the reliance on presumed functional forms or orbit libraries inherent in conventional DF- or orbit-based methods. Standing out with its flexibility, efficiency, and adeptness in managing observational effects,  $\text{EMPDF}$  warrants wide applications.

The key features of  $\text{EMPDF}$  include

- Minimal assumptions except for steady state. No assumptions are made on the specific form of the DF, and thus no free parameters in the DF construction under a given trial potential.
- Flexibility.  $\text{EMPDF}$  accommodates arbitrary DFs, including those with unbound orbits and substructures in orbital integrals, as long as the tracers are phase-mixed within the concerned volume.
- High precision. Tests demonstrate that  $\text{EMPDF}$  outperforms other minimal assumption methods and the Jeans equation (§3). The high efficiency also results in lower requirements for sample size and data quality.
- Effective treatment of observational effects.  $\text{EMPDF}$  treats selection functions (§2.3) and observational errors (§2.4) effectively. And it is robust against moderate observational errors even without explicit treatment (§3.4).
- Extendable framework. Though currently implemented for complete kinematics in spherical potentials, the concept of  $\text{EMPDF}$  can be applied for more general problems (§5).
- Useful by-product.  $\text{EMPDF}$  provides non-binned estimates of various statistics for the tracers, such as the energy distribution, number density, velocity dispersion, and anisotropy  $p(E)$ ,  $\varrho(r)$ ,  $\sigma(r)$ , and  $\beta(r)$ .

$\text{EMPDF}$  is a natural improvement upon the theoretical foundation of  $\text{oPDF}$  (Han et al. 2016a) but exploiting the full DF. It outperforms  $\text{oPDF}$  for small samples due to the smoothing of DF, whereas their performances become comparable when the sample size exceeds  $\sim 1000$ . This suggests that the information gained from the velocities beyond the spatial distribution used in  $\text{oPDF}$  is somehow limited. Nevertheless,  $\text{EMPDF}$  excels with small samples and provides a complete description of tracer kinematics with useful byproducts and an extendable framework.

$\text{EMPDF}$  can also be regarded as a lightweight Schwarzschild (1979) method. Instead of constructing an orbital library and solving for their weights under regulation, we obtain the orbital distribution directly and deterministically from the observed kinematics, with each tracer representing one orbit family. Thus,  $\text{EMPDF}$  has less computational complexity and parameter degeneracy compared to the Schwarzschild method.  $\text{EMPDF}$  is less model-dependent than presumed analytical or simulation-informed DFs. A particularity of our  $\text{EMPDF}$  is that it has the maximum flexibility allowing arbitrary DFs but without free parameters except for the potential well.

Interestingly, maximizing the likelihood of  $\text{EMPDF}$  is mathematically equivalent to minimizing the entropy of the action distributions of the tracers. The minimum entropy principle has been recently proposed for dynamical modeling by Beraldo e Silva et al. (2024) independently. Despite the mathematical resemblance, we argue that  $\text{EMPDF}$  has a stronger rationale based on the first principle of steady state, whereas the minimum entropy principle can be derived as a phenomenological result (§5.1). The perspective of  $\text{EMPDF}$  also allows for a natural treatment of observational effects.

We applied  $\text{EMPDF}$  to infer the MW mass profile using *Gaia* DR3 data of satellite galaxies and globular clusters separately (Fig. 7 and Table 1). Combining the two constraints yielded enclosed masses of  $26\pm 8$ ,  $46\pm 8$ ,  $90\pm 13$ , and  $149\pm 40 \times 10^{10} M_{\odot}$  for  $r < 30$ , 50, 100, and 200 kpc, respectively. These results align with the updated halo mass and concentration derived from the DF based on scaling relations of satellite kinematics in the Eagle simulation (Li et al. 2019, 2020a),  $M_{200c,\text{tot}} = 1.14\pm 0.15 \times 10^{12} M_{\odot}$  and  $c_{200c} = 11.5\pm 2.1$ , which give  $24\pm 4$ ,  $41\pm 6$ ,  $71\pm 9$ , and  $110\pm 13 \times 10^{10} M_{\odot}$  for the same radii. The simulation-informed DF offers superior precision owing to the additional information extracted from simulations, making the latter estimate one of the best current MW mass measurements. However, this method is limited to specific tracers such as satellite galaxies.

The MW mass profiles inferred by  $\text{EMPDF}$  are consistent with previous measurements in general (Fig. 8). We reiterate that the fitted parameters should be regarded as describing the local profile. In particular, the virial mass is not a complete or even a reliable description of the actual profile, because extrapolation based on local estimates can be risky. This may explain discrepancies in MW halo mass previously inferred from halo stars and satellite/GC tracers. We should focus on comparison within the radial range covered by tracers. Using multiple tracer populations with very different spatial distributions (e.g., halo stars and DGs) may help break the  $M$ - $c$  degeneracy (e.g., Walker & Peñarrubia 2011; Li et al. 2020a).

$\text{EMPDF}$  can also be used in combination with other information of tracer populations, such as chemical abundances or stellar ages. Dynamical modeling can be performed for different tracer populations separately (mono-abundance populations, Bovy et al. 2012; Bovy & Rix 2013; Ting et al. 2013; Mackereth & Bovy 2020) or for the joint chemodynamical distribution (extended distribution functions, Sanders & Binney 2015; Das & Binney 2016; Price-Whelan et al. 2021; Horta et al. 2024). This could provide stronger constraints and insights into the MW's chemodynamical structure in the future.

However, since  $\text{EMPDF}$  relies on the assumption of steady-state tracers and a static potential, it is subject to systematics when these assumptions are not met. Significant stochastic biases have been found in simulated tracers of various types (Han et al. 2016b; Wang et al. 2017, 2018; Han et al. 2020), in both galactic and cluster halos (Li et al. 2021, 2022). This concern becomes more severe when using the stars as tracers. Future exploration with more realistic mocks is worthwhile to gauge the level of such systematics. It is also possible to estimate the degree of deviation from equilibrium from observation (cf. Kipper et al. 2021). As for  $\text{EMPDF}$ , the difference between the best-fit empirical DF and observed kinematics itself provides useful diagnosis for deviations from steady-state, warranting future applications and explorations.

In particular, the LMC is believed to be a major perturber of the MW (e.g., Petersen & Peñarrubia 2020; Erkal et al. 2020; Kravtsov & Winney 2024), leading to deviations from equilibrium of the MW tracers. Correa Magnus & Vasiliev (2022) developed an orbit-rewinding method to compensate for LMC perturbations, where the corrected kinematics can be used with usual dynamical modeling methods that rely on equilibrium, including  $\text{EMPDF}$ .

## ACKNOWLEDGEMENTS

ZZL thanks Ling Zhu and Adrian M. Price-Whelan for the helpful discussion, and Eugene Vasiliev for the public pedagogical materials of dynamical modeling. This work was done on the GRAVITY supercomputer at the Department of Astronomy,

SJTU, and partially on the super cluster Moriah at HUJI. This work was supported in part by National Key R&D Program of China (2023YFA1607800, 2023YFA1607801, 2023YFA1605600, 2023YFA1605601), NSFC (12273021), the science research grants from the China Manned Space Project (No. CMS-CSST-2021-A03), 111 project (No. B20019) and the U.S. Department of Energy under grant DE-FG02-87ER40328 (YZQ). ZZL acknowledges the funding from the European Union’s Horizon 2020 research and innovation programme under the Marie Skłodowska-Curie grant agreement No. 101109759 (“CuspCore”) and the Israel Science Foundation Grant ISF 861/20. JH acknowledges the sponsorship from the Yangyang Development Fund.

This research made use of the following software: Agama (Vasiliev 2019), *astropy* (Astropy Collaboration et al. 2018), *Cython* (Behnel et al. 2011), *gs1* (Galassi et al. 2001), *Jupyter* (Granger & Perez 2021), *KDEpy* (Odland 2018), *Matplotlib* (Hunter 2007), *Numpy* (Harris et al. 2020), *ProPlot* (Davis 2021), *scikit-optimize* (Head et al. 2021), and *Scipy* (Virtanen et al. 2020). Some of the figures were created with the colorblind friendly scheme developed by Petroff (2021).

## DATA AVAILABILITY

The numerical implementation of *EMPDF* will be publicly available at <https://github.com/syrte/empdf>.

## REFERENCES

- Ablimit I., Zhao G., 2017, *ApJ*, **846**, 10
- Ablimit I., Zhao G., Flynn C., Bird S. A., 2020, *ApJ*, **895**, L12
- Acerbi L., 2018, *arXiv e-prints*, p. [arXiv:1810.05558](https://arxiv.org/abs/1810.05558)
- An J., Naik A. P., Evans N. W., Burrage C., 2021, *MNRAS*, **506**, 5721
- Archambeau C., Lee J. A., Verleysen M., 2003, in *ESANN 2003, European Symposium on Artificial Neural Networks*.
- Astropy Collaboration et al., 2018, *AJ*, **156**, 123
- Bahcall J. N., Tremaine S., 1981, *ApJ*, **244**, 805
- Behnel S., Bradshaw R., Citro C., Dalcin L., Seljebotn D. S., Smith K., 2011, *Computing in Science & Engineering*, **13**, 31
- Beloborodov A. M., Levin Y., 2004, *ApJ*, **613**, 224
- Beraldo e Silva L., Valluri M., Vasiliev E., Hattori K., de Siqueira Pedra W., Daniel K. J., 2024, *arXiv e-prints*, p. [arXiv:2407.07947](https://arxiv.org/abs/2407.07947)
- Binney J., 2014, *MNRAS*, **440**, 787
- Binney J., McMillan P., 2011, *MNRAS*, **413**, 1889
- Binney J., Tremaine S., 2008, *Galactic Dynamics: Second Edition*, 2nd edn. Princeton University Press, Princeton
- Binney J., Vasiliev E., 2023, *MNRAS*, **520**, 1832
- Bird S. A., et al., 2022, *MNRAS*, **516**, 731
- Bishop C. M., 2006, *Pattern Recognition and Machine Learning*. Springer, New York
- Bland-Hawthorn J., Gerhard O., 2016, *ARA&A*, **54**, 529
- Bobylev V. V., Baykova A. T., 2023, *Astronomy Reports*, **67**, 812
- Bovy J., Rix H.-W., 2013, *ApJ*, **779**, 115
- Bovy J., Murray I., Hogg D. W., 2010, *ApJ*, **711**, 1157
- Bovy J., Hogg D. W., Roweis S. T., 2011, *Annals of Applied Statistics*, **5**, 1657
- Bovy J., Rix H.-W., Liu C., Hogg D. W., Beers T. C., Lee Y. S., 2012, *ApJ*, **753**, 148
- Boylan-Kolchin M., Bullock J. S., Sohn S. T., Besla G., van der Marel R. P., 2013, *ApJ*, **768**, 140
- Bressan A., Marigo P., Girardi L., Salasnich B., Dal Cero C., Rubele S., Nanni A., 2012, *MNRAS*, **427**, 127
- Brooks R. A. N., Sanders J. L., Lilleengen S., Petersen M. S., Pontzen A., 2024, *MNRAS*, **532**, 2657
- Buckley M. R., Hogg D. W., Price-Whelan A. M., 2019, *arXiv e-prints*, p. [arXiv:1907.00987](https://arxiv.org/abs/1907.00987)
- Buckley M. R., Lim S. H., Putney E., Shih D., 2023, *MNRAS*, **521**, 5100
- Caldwell J. A. R., Ostriker J. P., 1981, *ApJ*, **251**, 61
- Callingham T. M., et al., 2019, *MNRAS*, **484**, 5453
- Cautun M., et al., 2020, *MNRAS*, **494**, 4291
- Chabrier G., 2001, *ApJ*, **554**, 1274
- Correa Magnus L., Vasiliev E., 2022, *MNRAS*, **511**, 2610
- Cuddeford P., 1991, *MNRAS*, **253**, 414
- Das P., Binney J., 2016, *MNRAS*, **460**, 1725
- Davis L. L. B., 2021, *ProPlot*, [doi:10.5281/zenodo.5602155](https://doi.org/10.5281/zenodo.5602155)
- Deason A. J., Fattahi A., Belokurov V., Evans N. W., Grand R. J. J., Marinacci F., Pakmor R., 2019, *MNRAS*, **485**, 3514
- Deason A. J., et al., 2021, *MNRAS*, **501**, 5964
- Dehnen W., Binney J., 1998, *MNRAS*, **294**, 429
- Dekel A., Ishai G., Dutton A. A., Maccio A. V., 2017, *MNRAS*, **468**, 1005
- Delaigle A., Meister A., 2008, *Bernoulli*, **14**, 562
- Dinh L., Sohl-Dickstein J., Bengio S., 2016, *arXiv e-prints*, p. [arXiv:1605.08803](https://arxiv.org/abs/1605.08803)
- Eadie G., Keller B., Harris W. E., 2018, *ApJ*, **865**, 72
- Eddington A. S., 1916, *MNRAS*, **76**, 572
- Eilers A.-C., Hogg D. W., Rix H.-W., Ness M. K., 2019, *ApJ*, **871**, 120
- El Gammal J., Schöneberg N., Torrado J., Fidler C., 2023, *J. Cosmology Astropart. Phys.*, **2023**, 021
- Erkal D., Belokurov V. A., Parkin D. L., 2020, *MNRAS*, **498**, 5574
- Evans N. W., Hafner R. M., de Zeeuw P. T., 1997, *MNRAS*, **286**, 315
- Evslin J., Del Popolo A., 2017, *ApJ*, **841**, 90
- Fardal M. A., van der Marel R. P., Law D. R., Sohn S. T., Sesar B., Hernitschek N., Rix H.-W., 2019, *MNRAS*, **483**, 4724
- Foreman-Mackey D., Hogg D. W., Lang D., Goodman J., 2013, *PASP*, **125**, 306
- Freundlich J., et al., 2020, *MNRAS*, **499**, 2912
- Fritz T. K., Di Cintio A., Battaglia G., Brook C., Taibi S., 2020, *MNRAS*, **494**, 5178
- Gaia Collaboration et al., 2016, *A&A*, **595**, A1
- Gaia Collaboration et al., 2018, *A&A*, **616**, A1
- Gaia Collaboration et al., 2023, *A&A*, **674**, A1
- Galassi M., et al., 2001, *GNU Scientific Library Reference Manual*. Network Theory Limited, Bristol
- Gerhard O. E., 1991, *MNRAS*, **250**, 812
- Gibbons S. L. J., Belokurov V., Evans N. W., 2014, *MNRAS*, **445**, 3788
- Gieles M., Zocchi A., 2015, *MNRAS*, **454**, 576
- Grand R. J. J., Deason A. J., White S. D. M., Simpson C. M., Gómez F. A., Marinacci F., Pakmor R., 2019, *MNRAS*, **487**, L72
- Granger B. E., Perez F., 2021, *Computing in Science and Engineering*, **23**, 7
- Gratton R., Bragaglia A., Carretta E., D’Orazi V., Lucatello S., Sollima A., 2019, *A&ARv*, **27**, 8
- Green G. M., Ting Y.-S., 2020, *arXiv e-prints*, p. [arXiv:2011.04673](https://arxiv.org/abs/2011.04673)
- Green G. M., Ting Y.-S., Kamdar H., 2023, *ApJ*, **942**, 26
- Han J., Wang W., Cole S., Frenk C. S., 2016a, *MNRAS*, **456**, 1003
- Han J., Wang W., Cole S., Frenk C. S., 2016b, *MNRAS*, **456**, 1017
- Han J., Wang W., Li Z., 2020, in Valluri M., Sellwood J. A., eds, *IAU Symposium Vol. 353, Galactic Dynamics in the Era of Large Surveys*. pp 109–112 ([arXiv:1909.02690](https://arxiv.org/abs/1909.02690)), [doi:10.1017/S1743921319008020](https://doi.org/10.1017/S1743921319008020)
- Harris C. R., et al., 2020, *Nature*, **585**, 357
- Head T., Kumar M., Nahrstaedt H., Louppe G., Shcherbaty I., 2021, *scikit-optimize/scikit-optimize*, [doi:10.5281/zenodo.5565057](https://doi.org/10.5281/zenodo.5565057)
- Helmi A., White S. D. M., 1999, *MNRAS*, **307**, 495
- Horta D., Price-Whelan A. M., Hogg D. W., Johnston K. V., Widrow L., Dalcanton J. J., Ness M. K., Hunt J. A. S., 2024, *ApJ*, **962**, 165
- Huang Y., et al., 2016, *MNRAS*, **463**, 2623
- Hunter J. D., 2007, *Computing in Science and Engineering*, **9**, 90
- Ibata R., et al., 2024, *ApJ*, **967**, 89
- Jethwa P., Erkal D., Belokurov V., 2016, *MNRAS*, **461**, 2212
- Jiao Y., Hammer F., Wang H., Wang J., Amram P., Chemin L., Yang Y., 2023, *A&A*, **678**, A208
- Jin C., Zhang Y., Balakrishnan S., Wainwright M. J., Jordan M. I., 2016, in Lee D. D., Sugiyama M., Luxburg U. V., Guyon I., Garnett R., eds, *Advances*

- in Neural Information Processing Systems 29. Curran Associates, Inc., pp 4116–4124
- Jing Y. P., 2000, *ApJ*, **535**, 30
- Kandasamy K., Schneider J., Póczos B., 2015, in Proceedings of the 24th International Conference on Artificial Intelligence. IJCAI'15. AAAI Press, Buenos Aires, Argentina, pp 3605–3611
- Karukes E. V., Benito M., Iocco F., Trotta R., Geringer-Sameth A., 2019, *J. Cosmology Astropart. Phys.*, 2019, 046
- Kent S. M., Gunn J. E., 1982, *AJ*, **87**, 945
- Kipper R., Tenjes P., Tempel E., de Proprijs R., 2021, *MNRAS*, **506**, 5559
- Koposov S., et al., 2008, *ApJ*, **686**, 279
- Kravtsov A., Winney S., 2024, *The Open Journal of Astrophysics*, **7**, 50
- Leonard P. J. T., Tremaine S., 1990, *ApJ*, **353**, 486
- Li Z.-Z., Han J., 2021, *ApJ*, **915**, L18
- Li Y.-S., White S. D. M., 2008, *MNRAS*, **384**, 1459
- Li Z.-Z., Jing Y. P., Qian Y.-Z., Yuan Z., Zhao D.-H., 2017, *ApJ*, **850**, 116
- Li Z.-Z., Qian Y.-Z., Han J., Wang W., Jing Y. P., 2019, *ApJ*, **886**, 69
- Li Z.-Z., Qian Y.-Z., Han J., Li T. S., Wang W., Jing Y. P., 2020a, *ApJ*, **894**, 10
- Li L., Shao Z., Li Z.-Z., Yu J., Zhong J., Chen L., 2020b, *ApJ*, **901**, 49
- Li Q., Han J., Wang W., Cui W., Li Z., Yang X., 2021, *MNRAS*, **505**, 3907
- Li Q., Han J., Wang W., Cui W., De Luca F., Yang X., Zhou Y., Shi R., 2022, *MNRAS*, **514**, 5890
- Li Z., Dekel A., Mandelker N., Freundlich J., François T. L., 2023, *MNRAS*, **518**, 5356
- Lim S. H., Raman K. A., Buckley M. R., Shih D., 2022, *arXiv e-prints*, p. [arXiv:2211.11765](https://arxiv.org/abs/2211.11765)
- Lim S. H., Putney E., Buckley M. R., Shih D., 2023, *arXiv e-prints*, p. [arXiv:2305.13358](https://arxiv.org/abs/2305.13358)
- Lokas E. L., Mamon G. A., 2003, *MNRAS*, **343**, 401
- Mackereth J. T., Bovy J., 2020, *MNRAS*, **492**, 3631
- Magorrian J., 2014, *MNRAS*, **437**, 2230
- Magorrian J., 2019, *MNRAS*, **484**, 1166
- Malhan K., Ibata R. A., 2019, *MNRAS*, **486**, 2995
- Manwadkar V., Kravtsov A. V., 2022, *MNRAS*, **516**, 3944
- Maronna R. A., Martin R. D., Yohai V. J., Salibián-Barrera M., 2019, *Robust Statistics: Theory and Methods* (with R). John Wiley & Sons
- McMillan P. J., 2017, *MNRAS*, **465**, 76
- McMillan P. J., Binney J., 2012, *MNRAS*, **419**, 2251
- Merritt D., 1985, *AJ*, **90**, 1027
- Michie R. W., Bodenheimer P. H., 1963, *MNRAS*, **126**, 269
- Nadler E. O., et al., 2020, *ApJ*, **893**, 48
- Naik A. P., An J., Burrage C., Evans N. W., 2022, *MNRAS*, **511**, 1609
- Navarro J. F., Frenk C. S., White S. D. M., 1996, *ApJ*, **462**, 563
- Necib L., Lin T., 2022, *ApJ*, **926**, 189
- Newton O., Cautun M., Jenkins A., Frenk C. S., Helly J. C., 2018, *MNRAS*, **479**, 2853
- Odland T., 2018, *tommyod/KDEpy: Kernel Density Estimation in Python*, [doi:10.5281/zenodo.2392268](https://doi.org/10.5281/zenodo.2392268)
- Osipkov L. P., 1979, *Soviet Astronomy Letters*, **5**, 42
- Ou X., Eilers A.-C., Necib L., Frebel A., 2024, *MNRAS*, **528**, 693
- Pace A. B., Erkal D., Li T. S., 2022, *ApJ*, **940**, 136
- Pardy S. A., et al., 2020, *MNRAS*, **492**, 1543
- Patel E., Besla G., Mandel K., Sohn S. T., 2018, *ApJ*, **857**, 78
- Peñarrubia J., Fattahi A., 2017, *MNRAS*, **468**, 1300
- Peñarrubia J., Koposov S. E., Walker M. G., 2012, *ApJ*, **760**, 2
- Peñarrubia J., Gómez F. A., Besla G., Erkal D., Ma Y.-Z., 2016, *MNRAS*, **456**, L54
- Petersen M. S., Peñarrubia J., 2020, *MNRAS*, **494**, L11
- Petroff M. A., 2021, *arXiv e-prints*, p. [arXiv:2107.02270](https://arxiv.org/abs/2107.02270)
- Posti L., Helmi A., 2019, *A&A*, **621**, A56
- Posti L., Binney J., Nipoti C., Ciotti L., 2015, *MNRAS*, **447**, 3060
- Price-Whelan A. M., et al., 2021, *ApJ*, **910**, 17
- Read J. I., et al., 2021, *MNRAS*, **501**, 978
- Rehmetulla N., Valluri M., Vasiliev E., 2022, *MNRAS*, **511**, 5536
- Reino S., Rossi E. M., Sanderson R. E., Sellentin E., Helmi A., Koppelman H. H., Sharma S., 2021, *MNRAS*, **502**, 4170
- Roche C., Necib L., Lin T., Ou X., Nguyen T., 2024, *arXiv e-prints*, p. [arXiv:2402.00108](https://arxiv.org/abs/2402.00108)
- Rothfuss J., Ferreira F., Walther S., Ulrich M., 2019, *arXiv e-prints*, p. [arXiv:1903.00954](https://arxiv.org/abs/1903.00954)
- Sanders J. L., Binney J., 2015, *MNRAS*, **449**, 3479
- Sanderson R. E., Helmi A., Hogg D. W., 2015, *ApJ*, **801**, 98
- Schaller M., et al., 2015, *MNRAS*, **451**, 1247
- Schwarzschild M., 1979, *ApJ*, **232**, 236
- Scott D. W., 1979, *Biometrika*, **66**, 605
- Scott D. W., 2015, *Multivariate Density Estimation: Theory, Practice, and Visualization*, 2nd edn. Wiley, Hoboken, New Jersey
- Sharma S., Steinmetz M., 2006, *MNRAS*, **373**, 1293
- Shen J., et al., 2022, *ApJ*, **925**, 1
- Silverman B. W., 1986, *Density Estimation for Statistics and Data Analysis*. Chapman and Hall, Boca Raton
- Simon J. D., 2019, *ARA&A*, **57**, 375
- Slizewski A., Dufresne X., Murdock K., Eadie G., Sanderson R., Wetzel A., Jurić M., 2022, *ApJ*, **924**, 131
- Smith M. C., et al., 2007, *MNRAS*, **379**, 755
- Sohn S. T., Watkins L. L., Fardal M. A., van der Marel R. P., Deason A. J., Besla G., Bellini A., 2018, *ApJ*, **862**, 52
- Speagle J. S., 2020, *MNRAS*, **493**, 3132
- Ting Y.-S., Rix H.-W., Bovy J., van de Ven G., 2013, *MNRAS*, **434**, 652
- Trick W. H., Bovy J., Rix H.-W., 2016, *ApJ*, **830**, 97
- Vasiliev E., 2018, *arXiv e-prints*, p. [arXiv:1802.08255](https://arxiv.org/abs/1802.08255)
- Vasiliev E., 2019, *MNRAS*, **482**, 1525
- Vasiliev E., Baumgardt H., 2021, *MNRAS*, **505**, 5978
- Vasiliev E., Valluri M., 2020, *ApJ*, **889**, 39
- Vasiliev E., Belokurov V., Erkal D., 2021, *MNRAS*, **501**, 2279
- Virtanen P., et al., 2020, *Nature Methods*, **17**, 261
- Walker M. G., Peñarrubia J., 2011, *ApJ*, **742**, 20
- Walker M. G., Mateo M., Olszewski E. W., Peñarrubia J., Evans N. W., Gilmore G., 2009, *ApJ*, **704**, 1274
- Walsh S. M., Willman B., Jerjen H., 2009, *AJ*, **137**, 450
- Wang W., Han J., Cooper A. P., Cole S., Frenk C., Lowing B., 2015a, *MNRAS*, **453**, 377
- Wang Y., Lin W., Pearce F. R., Lux H., Muldrew S. I., Onions J., 2015b, *ApJ*, **801**, 93
- Wang W., Han J., Cole S., Frenk C., Sawala T., 2017, *MNRAS*, **470**, 2351
- Wang W., Han J., Cole S., More S., Frenk C., Schaller M., 2018, *MNRAS*, **476**, 5669
- Wang W., Han J., Cautun M., Li Z., Ishigaki M. N., 2020, *Science China Physics, Mechanics, and Astronomy*, **63**, 109801
- Wang J., Hammer F., Yang Y., 2022a, *MNRAS*, **510**, 2242
- Wang W., et al., 2022b, *ApJ*, **941**, 108
- Wang H.-F., Chrobáková Ž., López-Corredoira M., Sylos Labini F., 2023, *ApJ*, **942**, 12
- Watkins L. L., Evans N. W., An J. H., 2010, *MNRAS*, **406**, 264
- Watkins L. L., van der Marel R. P., Sohn S. T., Evans N. W., 2019, *ApJ*, **873**, 118
- Webb J. J., Carlberg R. G., 2021, *MNRAS*, **502**, 4547
- Wegg C., Gerhard O., Bieth M., 2019, *MNRAS*, **485**, 3296
- Wilkinson M. I., Evans N. W., 1999, *MNRAS*, **310**, 645
- Wojtak R., Lokas E. L., Mamon G. A., Gottlöber S., Klypin A., Hoffman Y., 2008, *MNRAS*, **388**, 815
- Wolf J., Martinez G. D., Bullock J. S., Kaplinghat M., Geha M., Muñoz R. R., Simon J. D., Avedo F. F., 2010, *MNRAS*, **406**, 1220
- Xue X. X., et al., 2008, *ApJ*, **684**, 1143
- Yang M.-S., Lai C.-Y., Lin C.-Y., 2012, *Pattern Recognition*, **45**, 3950
- Yang T., Boruah S. S., Afshordi N., 2020, *MNRAS*, **493**, 3061
- Zhai M., Xue X.-X., Zhang L., Li C.-D., Zhao G., Yang C.-Q., 2018, *Research in Astronomy and Astrophysics*, **18**, 113
- Zhou Y., Li X., Huang Y., Zhang H., 2023, *ApJ*, **946**, 73
- Zhu L., et al., 2018, *MNRAS*, **473**, 3000
- van den Bosch R. C. E., van de Ven G., Verolme E. K., Cappellari M., de Zeeuw P. T., 2008, *MNRAS*, **385**, 647

## APPENDIX A: CONSTRUCTION OF EMPIRICAL DF

We construct the smooth orbital distribution  $p(E, L)$  from a given sample, largely following the procedure of Li et al. (2019), originally used for constructing the stacking orbital distribution of satellite galaxies in simulations.

The  $(E, L)$  are distributed in a sharp triangular shape unevenly, making it non-trivial to handle boundaries during smoothing. It is more convenient to perform this task in the parameter space of  $(E, \varepsilon^2)$ , where  $\varepsilon = L/L_{\max}(E) \in [0, 1]$  and  $L_{\max}(E)$  is the maximum angular momentum allowed for an orbit with energy  $E$ . Without observational limits,  $L_{\max}$  corresponds to the angular momentum of the circular orbit with given energy, and  $\varepsilon$  is known as *orbital circularity*. When considering tracers restricted within radius range  $[r_{\min}, r_{\max}]$ ,  $L_{\max}(E)$  becomes

$$L_{\max}(E) = \begin{cases} r_{\min} \sqrt{2[E - \Phi(r_{\min})]}, & r_{\text{cir}}(E) < r_{\min}, \\ \sqrt{GM(< r_{\text{cir}}) r_{\text{cir}}}, & r_{\min} \leq r_{\text{cir}}(E) \leq r_{\max}, \\ r_{\max} \sqrt{2[E - \Phi(r_{\max})]}, & r_{\max} < r_{\text{cir}}(E), \end{cases}$$

where  $r_{\text{cir}}$  is the radius of the circular orbit with energy  $E$ .

Given the trial potential, we calculate  $\{E_i, \varepsilon_i^2\}_{i=1}^N$  and their weights  $\{\omega_i\}$  (equal to 1 unless a selection function is involved). We then construct the smooth density distribution in  $(E, \varepsilon^2)$  space via KDE,

$$p(E, \varepsilon^2) = \frac{1}{\sum_{i=1}^N \omega_i} \sum_{i=1}^N \omega_i \mathcal{K}\left(\frac{E - E_i}{h\sigma_E}\right) \mathcal{K}\left(\frac{\varepsilon^2 - \varepsilon_i^2}{h\sigma_{\varepsilon^2}}\right), \quad (\text{A1})$$

where  $\sigma_E$  and  $\sigma_{\varepsilon^2}$  are the standard deviations of  $\{E_i\}$  and  $\{\varepsilon_i^2\}$  respectively, and  $h$  is the smoothing bandwidth.  $\mathcal{K}$  denotes the Gaussian smoothing kernel,  $\mathcal{K}(x/\sigma) = (\sqrt{2\pi}\sigma)^{-1} \exp[-(x/\sigma)^2/2]$ . We adopt Scott (1979)'s rule of thumb,

$$h = n_{\text{eff}}^{-1/(n_{\text{dim}}+4)}, \quad (\text{A2})$$

where  $n_{\text{dim}} = 2$  for 2D smoothing, and  $n_{\text{eff}} = (\sum \omega_i)^2 / (\sum \omega_i^2)$  is the effective sample size. The smoothing size is thus larger for a small sample or unequal weights. Reflecting boundaries are applied at  $\varepsilon^2 = 0$  and 1 and  $E = \Phi(r_{\min})$ . By construction,  $p(E, \varepsilon^2)$  satisfies  $\int_{\Phi(r_{\min})}^{\infty} \int_0^1 p(E, \varepsilon^2) dE d\varepsilon^2 = 1$ .

The orbital distribution and DF (Eq. 4) are then

$$p(E, L) = \frac{2L}{L_{\max}^2(E)} p(E, \varepsilon^2), \quad (\text{A3})$$

$$f_{\Phi}(\mathbf{r}, \mathbf{v}) = \frac{p(E, \varepsilon^2)}{4\pi^2 L_{\max}^2(E) T_r(E, L)}. \quad (\text{A4})$$

The DF  $f_{\Phi}$  is guaranteed to be a smooth function, since  $p(E, \varepsilon^2)$  is smoothed. Direct smoothing in  $f(E, L)$  is meaningless, because it does not conserve the mass [recall that  $f$  is a distribution in  $(x, \mathbf{v})$  rather than  $(E, L)$ ].

### A1 Additional remarks on KDE

KDE is a well-established technique with wide applications (Silverman 1986; Scott 2015). Theory and practice suggest that the bandwidth is more important than the specific choice of kernel. We find that the Scott rule is indeed close to optimal for our test cases. When the sample is very extended with long tails, standard deviation  $\sigma$  may overestimate the smoothing scale. A robust alternative is the normalized median absolute deviation (MADN, Maronna et al. 2019, p36),  $\hat{\sigma} = 1.4826 \text{ median}\{|x - \text{median}\{x\}|\}$ . Additional attention is needed to determine the best kernel size (e.g., using cross-validation)

for multimodal distributions, where Scott's rule is perhaps not optimal. We also tested adaptive smoothing size  $h$  based on  $k$ -nearest neighbor (see e.g., Li et al. 2019), but it yields worse performance.

Besides KDE, there are other techniques for density estimation that have potential or existing applications in dynamical modeling methods (not limited to EMPDF). Examples include binning with Voronoi tessellation or entropy-based binary decomposition (Sharma & Steinmetz 2006, EnBid), Gaussian mixtures (Magorrian 2014), penalized B-splines (Vasiliev 2018), neural networks (Rothfuss et al. 2019)<sup>16</sup>, and normalizing flows (Dinh et al. 2016; Lim et al. 2022). However, it is crucial to remember that dynamical modeling requires more than just smoothing for orbits within a specific potential. The chosen technique must also provide consistent and continuous density estimation (and thus likelihood) when changing the trial potential. The advantage of KDE on this point becomes more evident in the next subsection.

### A2 Comments on Magorrian 2014 and Gaussian mixtures

Magorrian (2014) proposed an elegant DF method based on Infinite Gaussian Mixture Models (GMMs) regulated by a Dirichlet process. It models the distribution of actions as the sum of Gaussian blobs whose number, weights, locations, and shapes are to be determined during fitting. There is a clear technical resemblance with EMPDF, as both construct orbital distribution (through GMMs vs KDE) and use likelihood in 6D phase space.

While mathematically elegant, Infinite GMMs face several practical challenges that hinder their general adoption for dynamical modeling. GMMs lack a closed-form solution and require iterative optimization (Bishop 2006), which is sensitive to initialization and can converge to undesired local optima (Archambeau et al. 2003; Yang et al. 2012; Jin et al. 2016). Moreover, GMMs may exhibit unpredictable variations in the number, location, and size of Gaussian blobs when the underlying potential changes, possibly leading to discontinuous likelihood and unreliable parameter inference (Magorrian 2014, Appendix C3). In contrast, KDE has no free parameters, and the resultant likelihood responds continuously to changes in potential. KDE also outperforms GMMs in computational efficiency, particularly for large datasets (e.g., by using fast Fourier transform).

More importantly, the underlying philosophy differs. Magorrian (2014) can be regarded as a highly flexible analytical model with many free parameters, whereas EMPDF considers the time-averaged DF of the tracers themselves deterministically.

## APPENDIX B: LIKELIHOOD AND KULLBACK-LEIBLER DIVERGENCE

To quantify the difference between the time-averaged DF and the instantaneous DF, a natural choice based on information theory is the Kullback-Leibler (KL) divergence (aka. relative entropy), a measure of how one probability distribution differs from another (Bishop 2006, §1.6.1). For two distributions  $p(x)$  and  $q(x)$ , the KL divergence from  $p$  to  $q$  is defined as

$$\text{KL}(q||p) = \int q(x) \ln \frac{q(x)}{p(x)} dx. \quad (\text{B1})$$

<sup>16</sup> [https://github.com/freelunchtheorem/Conditional\\_Density\\_Estimation](https://github.com/freelunchtheorem/Conditional_Density_Estimation)



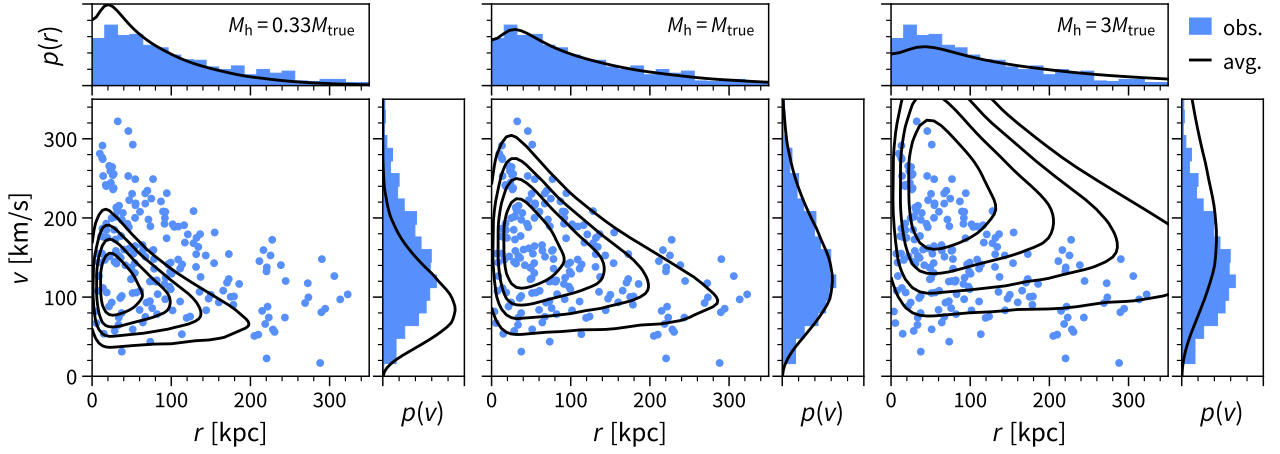


**Figure E1.** Similar to Fig. 2, but illustrating how the simulation-informed DF scales with the potential. The blue dots and shades show the observation data. The black contour and distributions represent the model predicted by the scaling relation.

Suppose that the data sample  $\{x_i\}$  was generated from an unknown distribution  $q(x)$  that we wish to approximate using some parametric distribution  $p(x|\Theta)$ , controlled by a set of parameters  $\Theta$ . Specifically, in our problem  $q$  is the underlying DF of the tracers represented by observation  $\{\mathbf{w}_i\}$ , and  $p$  is the empirical DF which depends on the parametrized potential.

One way to determine  $\Theta$  is to minimize the KL divergence between  $q(x)$  and  $p(x|\Theta)$ . Although we do not know  $q(x)$  explicitly, the integration over  $q(x)$  can be approximated by summing over  $x_i$ ,  $\text{KL}(q||p)_\Theta = \frac{1}{N} \sum_i [\ln q(x_i) - \ln p(x_i|\Theta)] = -\frac{1}{N} \sum_i \ln p(x_i|\Theta) + \text{const}$ , where ‘const’ arises because  $q(x)$  does not depend on  $\Theta$ . Therefore, minimizing KL divergence is equivalent to maximizing the log likelihood for  $\Theta$ ,  $\sum_i \ln p(x_i|\Theta)$ .

We should note that while the mathematical form of the KL divergence (or log likelihood) resembles entropy, their interpretations differ. Entropy measures the information of a single distribution, whereas KL divergence quantifies the difference between two distributions.

### APPENDIX C: SELF-CORRECTION FOR OBSERVATIONAL ERRORS

The observational errors will smear and bias the DF that is constructed empirically from observed kinematics using KDE. For example, the observed tangential velocity and thus angular momentum are on average biased to high, especially so for distant MW tracers (see e.g., Fig. 5 and 6 in Li et al. 2020a). The task is then to derive the underlying DF unbiasedly by removing (deconvolving) the scatters introduced by observational errors. Present efforts for error correction in density estimation are largely limited to homoscedastic problems, e.g., deconvolved KDE technique (Delaigle & Meister 2008; Bovy et al. 2011).<sup>17</sup> Here we propose a novel general method to correct heteroscedastic errors using *iterative reweighted importance sampling* (IRIS). It can be applied to other problems as well, e.g., the correction of the Eddington bias of galaxy luminosity functions.

If the underlying DF  $f(\mathbf{w})$  is known in prior, for an observed tracer

$\mathbf{w}_i$ , its true kinematics  $\mathbf{w}_{\text{tr}}$  is given by the posterior distribution,

$$p(\mathbf{w}_{\text{tr}}|\mathbf{w}_i) \propto p_{\text{err}}(\mathbf{w}_i|\mathbf{w}_{\text{tr}})f(\mathbf{w}_{\text{tr}}). \quad (\text{C1})$$

The key idea of the self-correction is that the sum of the posterior distributions of a tracer sample provides a much closer representation of the true DF than the direct observation  $\{\mathbf{w}_i\}$ .

The above posterior distribution can be achieved by importance sampling. For each tracer  $\mathbf{w}_i$ , we sample  $m$  subparticles  $\{\mathbf{w}_{ij}\}_{j=1}^m$  according to  $p(\mathbf{w}_{ij}) \propto p_{\text{err}}(\mathbf{w}_i|\mathbf{w}_{ij})$ , and assign weights as  $\omega_{ij} \propto f(\mathbf{w}_{ij})$ , with normalization  $\sum_j \omega_{ij} = 1$ . In this way,  $\{\mathbf{w}_{ij}, \omega_{ij}\}_j$  represents a weighted realization of Eq. (C1), and the ensemble  $\{\mathbf{w}_{ij}, \omega_{ij}\}_{i,j}$  provides a better representation of the underlying DF than the original  $\{\mathbf{w}_i\}_i$ .

Though we do not know the true DF  $f(\mathbf{w})$  in the beginning, we can resort to an iterative procedure to approach a self-consistent DF and largely remove the observation scatter. Starting with the empirical DF  $f(\mathbf{w})$  constructed from observed kinematics  $\{\mathbf{w}_i\}$  (Eq. 2) as a rough guess, we initialize  $\omega_{ij} \propto f(\mathbf{w}_{ij})$  (alternatively, initializing with  $\omega_{ij} = 1/m$  also works). We then rebuild  $f(\mathbf{w})$  from  $\{\mathbf{w}_{ij}, \omega_{ij}\}_{i,j}$ , and recompute  $\omega_{ij}$  by  $f(\mathbf{w})$  in iteration. For the KDE smoothing bandwidth, we use the Scott’s rule (Eq. A2) with the effective sample size,  $n_{\text{eff}} = (\sum_{ij} \omega_{ij})^2 / (\sum_{ij} \omega_{ij}^2)$ . Clearly, the computational cost of this scheme is significantly higher than in cases without observational error due to the large number of subparticles involved.<sup>18</sup>

Preliminary numerical experiments with 1D and 2D distributions confirm the viability of the above procedure. The underlying distribution can be closely recovered from a sample with large observational errors comparable to its intrinsic spread. Taking  $m = 1000$  with 10 iterations usually yields sufficiently accurate results, achieving approximate convergence, though these parameters may vary depending on the specific problem and dimension. Validation for actual dynamical modeling problems is left for future work.

When the selection function is also involved, we should replace the  $\omega_{ij}$  with  $\omega_{ij} \cdot \omega_{\text{sel}}(\mathbf{w}_{ij})$  to construct the empirical DF (Eq. 2), where  $\omega_{\text{sel}}(\mathbf{w}_{ij})$  is the correction factor for selection function (Eq. 7).<sup>19</sup>

<sup>17</sup> <https://github.com/jobovy/extreme-deconvolution>; cf. also <https://github.com/tholoien/XDGM>

<sup>18</sup> One may wonder if we can reduce the computation of KDE by using the mean posterior values  $\langle \mathbf{w}_{\text{tr}} \rangle_i = \sum_j \omega_{ij} \mathbf{w}_{ij}$  ( $N$  particles) instead of the ensemble subparticles  $\mathbf{w}_{ij}$  ( $N \times m$  subparticles) to construct the empirical DF. Unfortunately, this does not converge to the correct underlying distribution.

<sup>19</sup> A subtle note: a selection in observation might perform on the either

Besides the empirical DF, the observational errors also affect the likelihood (see Eq. 12),  $p_{\text{ob}}(\mathbf{w}_i | \Theta_{\Phi}) = \int p_{\text{err}}(\mathbf{w}_i | \mathbf{w}_{\text{tr}}) f_{\Phi}(\mathbf{w}) d^6 \mathbf{w}_{\text{tr}}$ . It is easy to compute the integral by Monte Carlo integration with importance sampling (Li et al. 2020a, §3.2),<sup>20</sup>

$$p_{\text{ob}}(\mathbf{w}_i | \Theta_{\Phi}) = \frac{1}{m} \sum_j f_{\Phi}(\mathbf{w}_{ij}). \quad (\text{C2})$$

#### APPENDIX D: SPHERICAL JEANS EQUATION

The spherical Jeans equation (BT08, eq. 4.214) writes,

$$\frac{d(v\sigma_r^2)}{vdr} + \frac{2\sigma_r^2}{r} \left(1 - \frac{\sigma_t^2}{2\sigma_r^2}\right) = -\frac{d\Phi}{dr} \quad (\text{D1})$$

where the tracer number density  $\nu$ , velocity dispersions  $\sigma_r^2 = \langle v_r^2 \rangle$  and  $\sigma_t^2 = \langle v_t^2 \rangle$ , and velocity anisotropy  $\beta = 1 - \sigma_t^2/2\sigma_r^2$  are functions of radius. These quantities are measured from observation. The mass within a given radius is thus

$$M(< r) = - \left[ \frac{d \ln(v\sigma_r^2)}{d \ln r} + 2\beta \right] \frac{r\sigma_r^2}{G}. \quad (\text{D2})$$

We adopt the ‘‘backward’’ implementation by Li et al. 2021. We divide the tracers into  $m$  radial bins ( $m = 5$  for  $N_{\text{tracers}} = 160$ , and 20 for larger sample size). In each bin, we measure  $\sigma_r^2, \sigma_t^2, \beta$  and  $\nu\sigma_r^2$ . The gradient of  $\nu\sigma_r^2$  is estimated by finite difference. We compute  $M_i$  for  $i$ -th bin using Eq. (D2) and determine the covariance matrix  $\Sigma_{ij} = \langle \delta M_i \delta M_j \rangle$  using bootstrap resampling of the tracers. For a given potential model, we calculate  $\hat{M}_i = M_{\text{model}}(< r_i)$ . We then search for parameters of the best-fit potential by minimizing  $\chi^2 = (\hat{M}_i - M_i) \Sigma_{ij}^{-1} (\hat{M}_j - M_j)$  with the Python package `IMINUIT`.<sup>21</sup>

This backward method offers more direct estimates of the mass profile but also suffers from observational errors directly and requires relatively large sample sizes. In contrast, the forward approach assumes some parametric form for the potential and tracer distribution, then computes expected velocity distributions. It can apply to small samples and handle observational errors and selection functions more effectively. Yet similar to analytical DF methods, improper model assumptions may lead to biases.

#### APPENDIX E: ILLUSTRATION OF SIMULATION-INFORMED DF

The simulation-informed DF method (Li et al. 2020a) assumes that the kinematics of tracers scale with the potential well. It constructs a template DF by rescaling and stacking halo tracers in simulations. The DF model for any virial mass and concentration is obtained by rescaling this template DF using the characteristic scales of the NFW potential,  $r_s$  and  $v_s$ . This scaling procedure is illustrated in Fig. E1, clarifying its difference from `EMPDF`. When applied to different potentials, the predicted distribution of simulation-informed DF changes more dramatically than `EMPDF` in response to variations

the true distance or the observed distance, depending how the sample is selected. The two cases have slightly different likelihood functions. The actual difference is usually negligible, so here we treat it as if the sample is selected by  $\mathbf{w}_{\text{tr}}$  for simplicity.

<sup>20</sup> Strictly speaking, Eq. (C2) differs from Eq. (12) by a constant factor (see footnote 5 in Li et al. 2020a), but this has no effect on the parameter inference.

<sup>21</sup> <https://github.com/scikit-hep/iminuit>

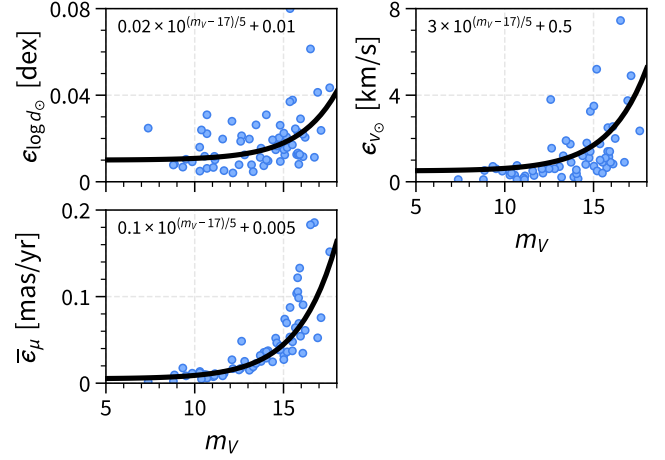


**Figure F1.** Observational errors of MW satellites and globular clusters with *Gaia* DR3 measurements. Blue symbols show the errors in Heliocentric distance  $d_{\odot}$ , proper motion  $\mu$ , and line-of-sight velocity  $v_{\text{los}}$  as functions of apparent magnitude for MW tracers within [20, 300]kpc. Black curves show the fitting relations according to the formulas in each panel.

in potential. This explains why `EMPDF` provides tighter constraints and exhibits a different parameter degeneracy direction.

#### APPENDIX F: MOCKING OBSERVATIONAL EFFECTS

Following §3.1, we generate mock tracers within [20, 300]kpc as the parent sample, on which we add the observational effects to mimic the MW satellite galaxies used in this work. For simplicity, we place the mock observer at the center of the halo, and thus the observables, Heliocentric distance  $d_{\odot}$ , proper motion  $\mu$ , and line-of-sight velocity  $v_{\text{los}}$ , become  $d_{\odot} = r$ ,  $\mu = v_t/r$ , and  $v_{\text{los}} = v_r$ , respectively.

**Selection function.** We mimic the MW satellites as a flux-limited sample, where tracers fainter than  $m_{V,\text{max}} = 17$  are unobservable (cf. Fig. 6). The maximal observable radius of a tracer with absolute magnitude  $M_V$  is then  $r_{\text{obs,max}}(M_V) = 10^{-0.2(M_V - 17 + 10)}$  kpc. The complete satellite luminosity function at faint end is  $N(< M_V) = 10^{0.156M_V + 2.21}$  (Newton et al. 2018). Using the mapping between  $M_V$  and  $r_{\text{obs,max}}$ , we obtain  $N(> r_{\text{obs,max}}) \propto r_{\text{obs,max}}^{-0.78}$ . Thus, the distribution of  $r_{\text{obs,max}}$  for MW satellites follows

$$p(r_{\text{obs,max}}) \propto r_{\text{obs,max}}^{-1.78}. \quad (\text{F1})$$

We assign each mock tracer with an  $r_{\text{obs,max}}$ , randomly sampled from  $p(r_{\text{obs,max}})$ . Tracers with  $r > r_{\text{obs,max}}$  are considered unobservable and removed from the mock sample.

**Observational error.** As shown in Fig. F1, typical observational errors in Heliocentric distance  $d_{\odot}$ , proper motion  $\mu$ , and line-of-sight velocity  $v_{\text{los}}$  of MW satellites (and globular clusters) with *Gaia* DR3 measurements can be approximated by

$$\epsilon_X = c_1 10^{0.2(m_V - 17)} + c_0 = c_1 r / r_{\text{obs,max}} + c_0, \quad (\text{F2})$$

where  $X = \log d_{\odot}, \mu$ , or  $v_{\text{los}}$ , and the parameters  $c_0$  and  $c_1$  are provided in the figure. The observational errors are assumed to be Gaussian and mutually independent. Random observational errors are added according to  $r/r_{\text{obs,max}}$  of each mock tracer following Eq. (F2).